Computers and Geotechnics 197 (2026) 108200

Contents lists available at ScienceDirect

Computers and Geotechnics

journal homepage: www.elsevier.com/locate/compgeo

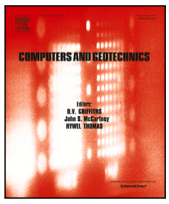

Research paper

Self-weight consolidation of kaolinite suspensions in deionized water measured by Nuclear Magnetic Resonance — experiments and modeling

Ismail Myouri [a,*], Nick Hol [b], Leo Pel [b], Claire Chassagne [a]

[a] Delft University of Technology, Faculty of Civil Engineering and Geosciences, Environmental Fluid Mechanics, Box 5048, 2600 GA, Delft, The Netherlands
[b] Eindhoven University of Technology, Department of Applied Physics, Transport in Permeable Media, P.O. Box 513, 5600 MB Eindhoven, The Netherlands

ARTICLE INFO

Keywords:
Large-strain consolidation
Self-weight consolidation
Numerical Modeling
Fine-grained soils
Constitutive modeling
Nuclear magnetic resonance

ABSTRACT

In this article, we study the self-weight consolidation behavior of kaolinite suspensions with different concentrations in deionized water using nuclear magnetic resonance (NMR). NMR enables the direct assessment of density distributions and pore size within the consolidating suspensions. The results show that electrochemical conditions (pH and ionic strength), arising from ion leaching from the kaolinite, influence the consolidation dynamics, in agreement with previous studies. The evolution of the density profile over time is interpreted using a large-strain consolidation model based on the Gibson–Merckelbach formulation. The model is implemented in both Eulerian and Lagrangian frameworks, allowing a comparison between these two approaches. A key observation from the NMR measurements is that the solid volume fraction reaches a maximum value at the base of the column. This behavior is not captured by the classical Merckelbach–Kranenburg constitutive model, highlighting its limitations in highly compacted regimes. To account for this effect, a simple modification based on a reduction in permeability is introduced. This modification can be interpreted as a hydraulic limitation, as it leads to vanishing fluid fluxes and prevents further densification. The comparison between experimental and numerical results shows that this approach improves the agreement with the measured density profiles. In addition, the model captures the main trends of the pore size distribution measured by NMR, although some discrepancies remain in magnitude. Overall, the combined experimental–numerical approach provides new insight into the applicability and limitations of Gibson–Merckelbach consolidation models for fine-grained suspensions.

1. Introduction

Dewatering and consolidation of "soft slurries", i.e. clayey materials with a high water content such as dredged sediments, is an ongoing topic of interest. These slurries, once consolidated into stress-bearing materials, are nowadays being considered for structural uses such as dike construction or land reclamation. Parameters of interest to engineers include dewatering and consolidation time, as well as the final physical properties of the bed (permeability, strength). These parameters strongly depend on material properties such as clay type, water content, pH, salinity, and organic matter type (Rial, 2019; Wang et al., 2023; Geng et al., 2022). Establishing the link between physical parameters and (bio)chemical properties is therefore essential for a proper estimation of the time evolution of the material behavior.

At high water content, soft slurries can be described as clay suspensions made of charged colloidal platelets (or stacks of platelets) that interact with each other and with ions and organic matter in the surrounding medium. At specific ionic concentrations and pH values, these interactions lead to aggregation (flocculation) (Russel et al., 1989; Dhont, 1996; Lagaly and Dékány, 2013). Aggregated particles, also known as flocs, can reach sizes several orders of magnitude larger than the original particles under suitable environmental conditions (hydrodynamics, residence time, pH, salinity) (Adachi and Tanaka, 1997; Schofield and Samson, 1954). In low-turbulence environments, such as dewatering basins, suspended particles gradually settle under gravity to form a connected structure at the bottom of the basin. Many studies focus on the influence of environmental conditions on the flocculation and settling phases of "mud" (i.e. clayey suspensions) (Ali and Chassagne, 2022; Abolfazli et al., 2024; Schofield and Samson, 1954). More recently, the influence of electrochemical conditions such as pore-fluid salinity has been investigated more systematically. For instance, Tafili et al. (2026) studied the effect of salt concentration on the mechanical behavior of kaolin through oedometer and triaxial tests. Their results show that increasing ionic strength leads to a reduction in void ratio and modifies the compressibility and strength of the material,

* Corresponding author.
E-mail address: imyouri@tudelft.nl (I. Myouri).

https://doi.org/10.1016/j.compgeo.2026.108200
Received 5 January 2026; Received in revised form 14 April 2026; Accepted 25 April 2026
Available online 11 May 2026

highlighting the strong influence of electrochemical conditions on soil structure and behavior. In the present study, these electrochemical effects are not introduced through controlled chemical conditions, but are instead captured indirectly through macroscopic parameters calibrated against NMR measurements in settling column experiments. This approach provides complementary insight by linking high-resolution experimental observations to classical consolidation models.

The changes in density over height and time within the connected structure are referred to as self-weight consolidation. In laboratory experiments, settling column experiments are commonly used to study the settling and consolidation behavior of slurries (Almabruk, 2018; Hurley, 1999). In such closed systems, return flow significantly reduces the settling velocity of suspended particles and corresponds to what is known as hindered settling. Simple analytical theories, such as the well-established Richardson and Zaki model, can be used to describe the hindered settling phase (Richardson and Zaki, 1997).

The influence of mud composition (clay type, organic matter content, ionic strength, pH) on consolidation behavior has been widely studied in geotechnical engineering, in particular through oedometer experiments (Barden, 1968; Robinson and Allam, 1998; Watabe et al., 2011; Zanin et al., 2021). These experiments rely on the assumption of small deformations of the soil matrix and are commonly interpreted using Terzaghi's theory (Terzaghi, 1925). However, this theory is not suitable for modeling self-weight consolidation of soft materials, which clearly exhibit large strains. Over the years, several alternatives have been proposed to address these limitations (Schiffman and Gibson, 1964; Davis and Raymond, 1965; Mikasa, 1963). In 1967, Gibson and RE (1967) introduced a comprehensive one-dimensional consolidation theory that accounts for self-weight effects, permeability variations with void ratio (or solid volume fraction), and the nonlinear relationship between effective stress and void ratio. This theory is applicable over a wide range of strains and is therefore well suited for soft slurries.

Numerous studies (Rial, 2019; François and Corda, 2022) have investigated large-strain consolidation of soft slurries by measuring permeability and density evolution over time using settling columns equipped with pore pressure sensors. In a more direct approach, Been and Sills (1981) introduced a non-destructive X-ray scanning technique to observe density changes along the height of the column. This method is often combined with pore pressure measurements and settlement monitoring (G. Bartholomeeusen, 2003; G.S. Bartholomeeusen, 2003). Most studies focus on natural mud collected in situ. It has been shown that large-strain theory can reasonably predict the time evolution of consolidation behavior (Been and Sills, 1981; Merckelbach and Kranenburg, 2002), with model parameters related to permeability and effective stress.

An alternative to X-ray scanning is nuclear magnetic resonance (NMR), which is also a non-destructive technique capable of measuring density changes over time and height. In addition, NMR can directly provide information on pore size (Hol et al., 2024; N.J. Hol et al., 2025). This technique is used in the present study.

In the experiments presented here, no organic matter is present. NMR measurements are performed on different kaolinite suspensions in water. Kaolinite is selected due to its well-characterized surface properties, which facilitate the interpretation of sedimentation data in terms of particle interactions. Kaolinite particles are micrometer-sized, hexagonal platelets (or stacks) with negatively charged surfaces and pH-dependent edge charges. Different microstructures are expected after settling, depending on platelet orientation, which is influenced by pH and ionic strength (Lagaly and Dékány, 2013). In particular, at low electrolyte concentrations, particles tend to form edge-to-face structures under acidic conditions, while more compact face-to-face arrangements are expected at basic pH (Brindley, 1958; Lagaly and Dékány, 2013).

In the following sections, both experimental results and theoretical modeling are presented. Density, pore size, and settlement of kaolinite suspensions with different initial concentrations are monitored using NMR in a small settling column. Electrophoretic mobility and particle size are measured prior to each experiment using dynamic light scattering (Ali et al., 2022; Shakeel et al., 2022), together with pH and conductivity. The consolidation process is modeled as a one-dimensional problem using the Gibson equation (Gibson and RE, 1967), formulated in both Eulerian and Lagrangian reference frames with the solid volume fraction as the main variable. The constitutive relations proposed by Merckelbach and Kranenburg (2002) are used to describe the relationship between effective stress, permeability, and solid volume fraction.

The objective of this work is not to introduce a new consolidation model, but to assess the applicability of large-strain formulations combined with the fractal constitutive model of Gibson and RE (1967) using high-resolution NMR measurements. The combined experimental–numerical approach allows a direct comparison between model predictions and measured density and pore-size profiles. This approach highlights limitations of the Gibson–Merckelbach framework, particularly in highly compacted regimes where a maximum solid volume fraction is observed experimentally but not reproduced by the model. The study also provides insight into the transition between settling and consolidation, as well as the influence of electrochemical conditions on consolidation behavior.

2. Large strain consolidation theory

In this part, we present the large-strain model used to determine the consolidated clay parameters (final solid volume fraction, permeability, and effective stress). This model was introduced by Merckelbach and Kranenburg (2002), based on the earlier work of Gibson (Gibson and RE, 1967).

We consider a settling column in which micrometric (kaolinite) particles are suspended in water. The particles settle and form a connected structure at the bottom of the column, which then consolidates under its own weight. The strains are considered to be large, as observed in earlier experimental investigations (Roscoe et al., 1958). The two parameters that describe consolidation in the model are the effective stress and the hydraulic conductivity of the connected structure.

In this framework, the material is assumed to form a continuous particle network, which allows the definition of an effective stress and a consolidation process driven by pore water pressure dissipation. This assumption is central to the formulation and defines the range of validity of the model.

The large-strain theory is based on the following assumptions:

1. The connected structure is saturated and consists of a compressible soil matrix and an incompressible pore fluid.
2. While the soil matrix is considered compressible, individual soil particles are incompressible.
3. Pore fluid flow velocities are small and governed by Darcy's law.
4. There is a unique relationship between soil permeability and solid volume fraction (or void ratio).
5. There is a unique relationship between vertical effective stress and solid volume fraction (or void ratio).
6. The material is homogeneous.

2.1. Darcy's law

As consolidation progresses over time, the solid particles (s) settle downward, while, by conservation of volume, water (w) moves upward. The flux of expelled water depends on the hydraulic conductivity, denoted K (m/s). The hydraulic conductivity is related to permeability through $K = k\rho_w g/\eta$, where k (m^2) is the permeability, ρ_w (kg/m^3) is the water density, g (m/s^2) is the gravitational acceleration, and η (Pa s) is the dynamic viscosity.

The relation between the flux of water through a porous medium and the hydraulic conductivity is expressed by Darcy's law:

$$J_{w/s} = -K\nabla h \tag{1}$$

where h (m) is the hydraulic head and $J_{w/s}$ (m/s) is the flux of water relative to the solid phase. This law can be expressed in either the Eulerian or the Lagrangian frame. In this work, the Eulerian frame is used.

Using the definition of the hydraulic head and taking z as the vertical coordinate (with the gravitational acceleration defined as $\vec{g} = -g\vec{e_z}$, where $\vec{e_z}$ is the unit vector in the z direction), Darcy's law becomes:

$$J_{w/s} = -K\frac{\partial}{\partial z}\left(z + \frac{P_w}{\rho_w g}\right) \tag{2}$$

where P_w (Pa) is the water pressure.

Terzaghi's principle yields (Terzaghi, 1925):

$$\sigma_{\text{tot}} = \sigma_{\text{sk}} + P_w \tag{3}$$

where σ_{tot} (Pa) is the total stress (which reduces to a vertical pressure in the one-dimensional case considered here), and σ_{sk} (Pa) is the effective stress (also reducing to a pressure in one dimension).

The balance of forces (neglecting acceleration) yields:

$$\frac{\partial \sigma_{\text{tot}}}{\partial z} + \rho g = 0 \tag{4}$$

where ρ (kg/m^3) is the density of the mixture of particles and water. This density is given by $\rho = \phi_s\rho_s + (1-\phi_s)\rho_w$, where ϕ_s is the solid volume fraction and ρ_s (kg/m^3) is the solid density.

Combining Eqs. (2), (3), (4) gives:

$$J_{w/s} = \frac{K}{\rho_w g}\left(\frac{\partial \sigma_{\text{sk}}}{\partial z} + (\rho_s - \rho_w)g\phi_s\right) \tag{5}$$

2.2. Continuity equation

In the absence of sources or sinks, the amount of particles within an elementary control volume depends only on the incoming and outgoing mass fluxes. This can be expressed mathematically as:

$$\frac{\partial \phi_s}{\partial t} = -\frac{\partial(\phi_s v_{s/lab})}{\partial z} \tag{6}$$

where $v_{s/lab}$ (m/s) is the velocity of the solid phase in the laboratory reference frame.

2.3. Gibson's equation

2.3.1. Eulerian frame formulation

For the undrained case, where there is no exchange of matter with the surroundings of the settling column, the sum of the fluxes at any position in the column must be equal to zero:

$$J_{w/lab} + J_{s/lab} = 0 \tag{7}$$

where $J_{w/lab}$ (m/s) is the flux of water in the laboratory reference frame.

By definition of the fluxes, Eq. (7) becomes:

$$\phi_w v_{w/lab} + \phi_s v_{s/lab} = 0 \tag{8}$$

Rewriting the previous equation using the relation $v_{w/s} = v_{w/lab} - v_{s/lab}$, one obtains:

$$\phi_w v_{w/s} = -v_{s/lab} \tag{9}$$

where $v_{w/s}$ is the velocity of water in the reference frame of the moving solid particles.

By combining Eqs. (5), (6), (9), one obtains the Gibson equation in the Eulerian frame:

$$\frac{\partial \phi_s}{\partial t} = \frac{\partial}{\partial z}\left[J_{\text{dif}}(\phi_s) + J_{\text{adv}}(\phi_s)\right] \tag{10}$$

This equation is an advection–diffusion partial differential equation, where the diffusion and advection fluxes are given by:

$$J_{\text{dif}}(\phi_s) = \frac{K(\phi_s)}{g\rho_w}\frac{\partial \sigma_{sk}(\phi_s)}{\partial \phi_s}\frac{\partial \phi_s}{\partial z}\phi_s \tag{11}$$

$$J_{\text{adv}}(\phi_s) = \frac{K(\phi_s)}{g\rho_w}(\rho_s - \rho_w)g\,\phi_s^2 \tag{12}$$

The advection flux J_{adv} (m/s) is driven by gravity, while the diffusion flux J_{dif} (m/s) results from contact forces between particles.

2.3.2. Lagrange frame and material coordinates

The Gibson equation Eq. (10) can also be expressed in terms of a time-dependent coordinate system that moves with the solid particles (see Appendix A for more details). The expression of the Gibson equation in this Lagrange frame is given by :

$$\left(\frac{\partial \phi_s}{\partial t}\right)_{z_{vol}} = \phi_s^2\frac{\partial}{\partial z_{vol}}\left(\frac{K(\phi_s)}{\rho_w g}\phi_s\left(\frac{\partial \sigma_{sk}(\phi_s)}{\partial z_{vol}} + (\rho_s - \rho_w)g\right)\right) \tag{13}$$

where z_{vol}(m) is the material coordinate that corresponds to the amount of solid mass in an elementary volume at time t, and which is defined as :

$$dz_{vol} = \phi_s\,dz = \phi_0\,da \tag{14}$$

where ϕ_0 is the initial solid volume fraction, ϕ_s is the solid volume fraction at a time $t > 0$, and a is the coordinate of the position z at time $t = 0$.

2.4. Initial and boundary conditions

The Gibson equations in both Eulerian and Lagrange formulations are linear parabolic differential equations. In order to have a well-posed problem, the set of equations needs to be completed by one initial condition at all spatial points and two spatial boundary conditions (one at the top and one at the bottom), at all times. In the case of an undrained settling column, the initial and boundary conditions are taken as follows:

Initial conditions we assume that the initial concentration is homogeneous in the column in both Eulerian and Lagrange reference frameworks. At any position in the column, the initial solid volume fraction ϕ_0 is the same:

$$\forall z \quad \phi_s(z, t=0) = \phi_0 \tag{15}$$

Boundary conditions The formulation of the boundary conditions depends on the chosen framework (see Fig. 1). In the Eulerian frame, the boundary conditions at the top and bottom are expressed in terms of solid fluxes. Since the column is undrained and no additional mass enters or leaves the column, the total solid flux is zero at the boundaries. The fluxes J_{adv} and J_{dif} denote the advective and diffusive solid fluxes, respectively, and are defined as

$$J_{dif}(\phi_s) = \frac{K(\phi_s)}{\rho_w g}\frac{\partial \sigma_{sk}(\phi_s)}{\partial \phi_s}\frac{\partial \phi_s}{\partial z}\phi_s \tag{16}$$

$$J_{adv}(\phi_s) = \frac{K(\phi_s)}{\rho_w g}(\rho_s - \rho_w)g\,\phi_s^2 \tag{17}$$

where $K(\phi_s)$ is the permeability and $\sigma_{sk}(\phi_s)$ is the effective stress. These terms represent, respectively, the flux driven by effective stress gradients and the flux driven by gravity.

$$\forall t > 0 \quad J_{adv}(z=0,t) = 0 \tag{18}$$

$$\forall t > 0 \quad J_{dif}(z=0,t) = 0 \tag{19}$$

$$\forall t > 0 \quad J_{adv}(z=H,t) = 0 \tag{20}$$

$$\forall t > 0 \quad J_{dif}(z=H,t) = 0 \tag{21}$$

where $z = H$ is the position of the liquid/air interface and $z = 0$ is the slurry/bottom interface of the column.

In the Lagrange frame, the boundary conditions are different. The boundary condition at the top is related to loading. In the present case,

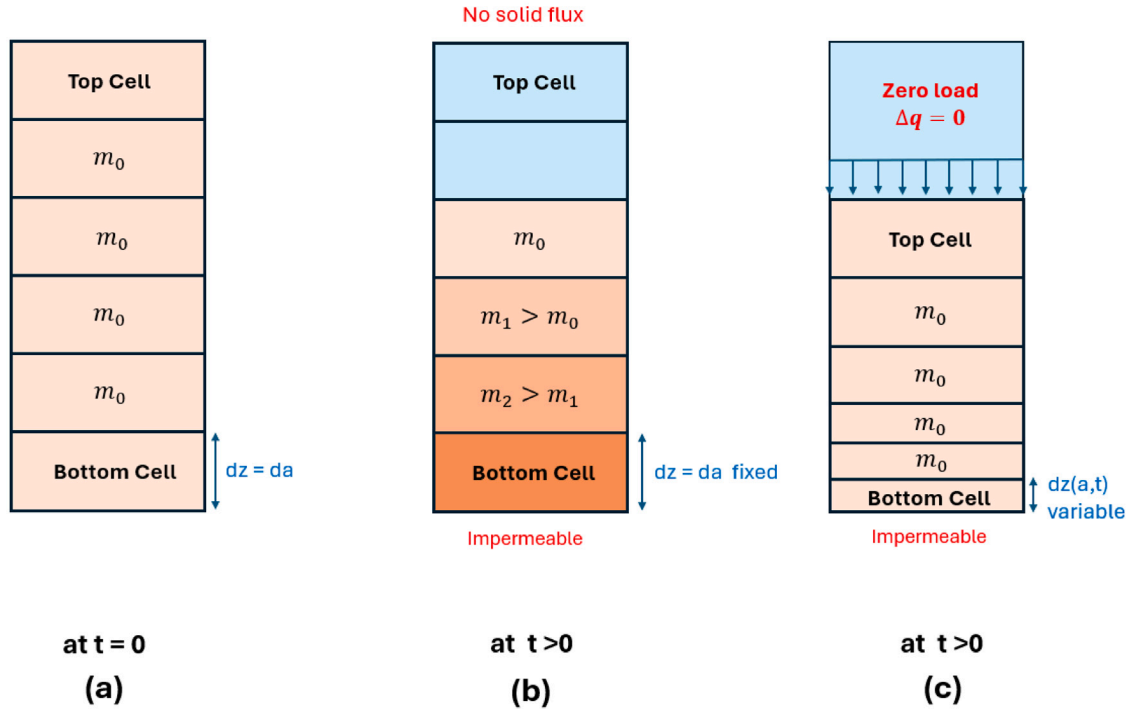

Fig. 1. Schematic representation of the main differences in boundary conditions between Euler and Lagrange formulations in a settling column: (a) initial condition with an initial solid volume fraction of $\phi_0 = m_0/(V_0\rho_s)$, where m_0 is the mass of particles in a cell and V_0 is the volume of one cell. At the start, all cells have the same volume. (b) Boundary conditions of the same column at time t in the Eulerian frame with fixed coordinate z. The suspension/bed interface is located between the cell containing m_0 particles and the cell containing m_1 particles. (c) Boundary conditions of the same column at time t in the Lagrange frame with material coordinate a. All cells contain m_0 particles and the solid volume fraction is calculated by adjusting the size of each cell.

no load is applied at the top, and therefore the solid volume fraction remains equal to its initial value. If a load is applied, the corresponding solid volume fraction should be obtained from the effective stress constitutive relation. At the bottom of the column, no drainage is allowed, which implies that the gradient of the pore water pressure is zero.

These boundary conditions for the Lagrange formulation are written as

$$\forall t > 0 \quad \frac{\partial}{\partial a}\left(\rho_w g z + P_w\right)\Big|_{a=0} = 0 \tag{22}$$

$$\forall t > 0 \quad \phi_s(a = H, t) = \phi_0 \quad \text{since } \sigma_{sk}(a = H, t) = 0 \tag{23}$$

where a denotes the material coordinate and P_w is the pore water pressure.

2.5. Effective stress and permeability relation

The mathematical model of Merckelbach and Kranenburg (2002) is based on the concept of space-filling fractal flocs, as illustrated in Fig. 2. This approach makes it possible to use the properties of fractals (in particular the fact that their density decreases with size) to derive expressions for both permeability and effective stress (see Eqs. (30) and (33)). A detailed discussion of the model is provided in Chapter 10 (p. 169) of Chassagne (2021).

We emphasize that the fractal description, although elegant, is only a mathematical framework, and there is no physical reason for flocs or soil particles to strictly behave as fractals. In particular, if the settling column contains "real" fractal flocs, the associated "mathematical" fractal flocs will not necessarily have the same fractal dimension.

As the "mathematical" flocs are space-filling, it follows that, for a given height z, the solid volume fraction is equal to the solid volume fraction inside a floc, hence:

$$\phi_s = \lambda_0 N \left(\frac{R_p}{R_N}\right)^3 \tag{24}$$

where λ_0 is a constant, N is the number of solid particles of size R_p within a floc of size R_N. The number of particles within a floc is given by:

$$N = \left(\frac{R_N}{R_p}\right)^{D_f} \tag{25}$$

where $D_f < 3$ is the fractal dimension. The relation between the solid volume fraction and the "mathematical" floc radius is thus:

$$\phi_s = \lambda_1 R_N^{(D_f-3)} \tag{26}$$

where λ_1 is a constant defined as $\lambda_1 = \frac{\lambda_0}{R_p^{(D_f-3)}}$.

For a homogeneous suspension at the initial time $t = 0$, one obtains:

$$\lambda_1 = \frac{\phi_0}{R_{N0}^{(D_f-3)}} \tag{27}$$

where $R_{N0} = R_N(z, t = 0)$ is the initial pore size, and ϕ_0 is the initial solid volume fraction, assumed to be uniform. Substituting λ_1 into Eq. (26) gives the key relation for the pore size:

$$R_N(z,t) = R_{N0}\left(\frac{\phi_s}{\phi_0}\right)^{\frac{1}{D_f-3}} \tag{28}$$

This relation is derived under the assumption of space-filling fractal flocs and therefore represents an idealized description of the pore structure. Its validity for the present material is assessed later through comparison with NMR measurements.

As time progresses, particles settle under gravity and the solid volume fraction increases at the bottom of the column. According to Eq. (26), a higher solid volume fraction leads to a smaller floc radius R_N for a given D_f (see Fig. 2(c)). An important feature of the model is that there is no mathematical discontinuity between the settling and consolidation regimes, and both can be described using the same constitutive relations for hydraulic conductivity and effective stress. In

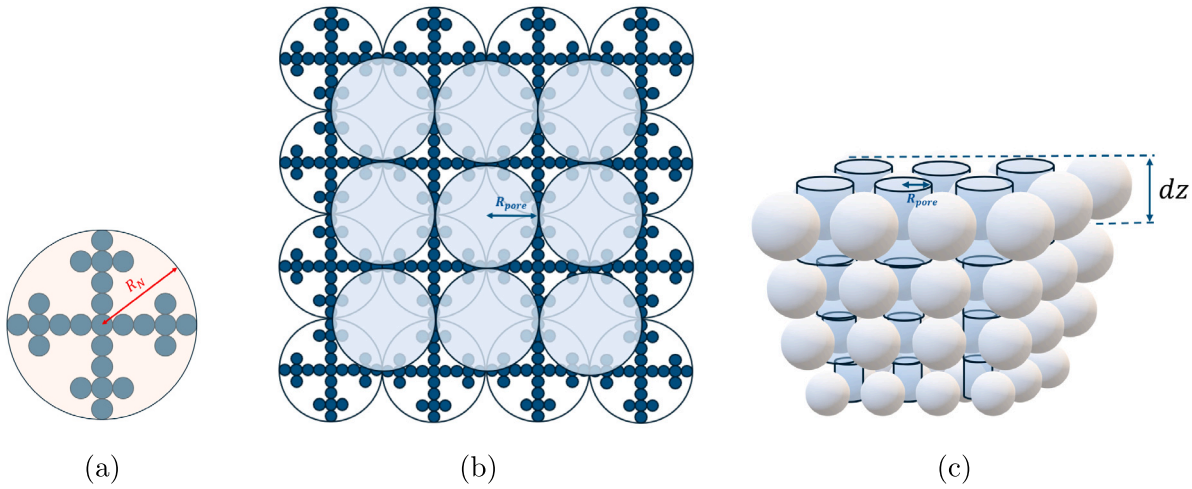

Fig. 2. Schematic representation of the mathematical fractal floc framework as presented by Merckelbach and Kranenburg (2002): (a) schematic representation of a mathematical fractal floc of size $R_N(z)$ containing N particles of size R_0; (b) schematic representation of connecting pores at a given height z, with $R_{\text{pore}}(z) \approx R_N(z)$; (c) three-dimensional schematic representation of flocs and pores as a function of height z.

the settling regime, all (space-filling) "mathematical" flocs have the same size, determined by the initial volume fraction and R_0. In the consolidation regime, the floc size evolves with $\phi_s(z)$, decreasing as ϕ_s increases toward the bottom of the column.

To derive an expression for the hydraulic conductivity, Merckelbach and Kranenburg (2002) used the Poiseuille relation (Poiseuille, 1844), which relates permeability to the square of the pore radius:

$$K(\phi_s) \sim R_N^2 \tag{29}$$

Using Eqs. (26) and (29), they define:

$$K(\phi_s) = K_k \phi_s^{-n} \tag{30}$$

where K_k is a fitting parameter and $n = 2/(3 - D_f)$.

The effective stress is derived from the observation that the number of bonds per floc (i.e. the number of contacts with neighboring flocs) does not depend on floc size, which is a property of fractals. The total number of bonds per unit area N_{total} is therefore:

$$N_{\text{total}} = \frac{N_0}{R_N^2} \tag{31}$$

where N_0 is the number of bonds per floc. The effective stress is assumed to be proportional to this quantity:

$$\sigma_{sk} \sim N_{\text{total}} \tag{32}$$

Using Eqs. (26) and (31), one obtains:

$$\sigma_{sk}(\phi_s) = K_\sigma \phi_s^n \tag{33}$$

where K_σ is a fitting parameter.

It is important to recall that the Gibson–Merckelbach formulation assumes continuous particle contact, which allows the definition of an effective stress and a consolidation process driven by pore water pressure dissipation. The implications of this assumption are discussed later in the context of dilute suspensions.

2.6. Numerical solution

Both the Eulerian and Lagrangian formulations are solved numerically using two different methods. The consolidation problem defined in the Eulerian framework is solved using the finite volume method (FVM), while the same problem formulated in the Lagrangian framework is solved using the finite difference method (FDM).

The two models provide similar results as long as the diffusion flux terms remain small. When these fluxes become significant, a density gradient (i.e. a diffusion layer) develops at the water/slurry interface in the Eulerian model, which is not observed in the Lagrangian model. This difference is not due to numerical instabilities, but arises from the different boundary conditions imposed in each framework. This can be understood by deriving the analytical final consolidation profile in the Eulerian framework (Merckelbach and Kranenburg, 2002; Chassagne, 2019), given by:

$$\phi_\infty(z) = \phi_\infty(z=0)\left[1 - \frac{z}{h_\infty}\right]^{\frac{1}{n-1}} \tag{34}$$

where:

$$\phi_\infty(z=0) = \left[\frac{\phi_0 H(\rho_s - \rho_w)g}{K_\sigma}\right]^{\frac{1}{n}} \tag{35}$$

and

$$h_\infty = \frac{n}{(n-1)}\frac{\phi_0}{\phi_\infty(z=0)}H \tag{36}$$

In the Lagrangian framework, the final solution can be expressed as a function of the initial coordinate Z:

$$\sigma_{sk,\infty}(Z) = \phi_0(\rho_s - \rho_w)g(H_0 - a), \tag{37}$$

which leads to:

$$\phi_\infty(a) = \left(\phi_0^n + \frac{\sigma_{sk,\infty}(a)}{K_\sigma}\right)^{1/n}. \tag{38}$$

The corresponding Eulerian profile can then be obtained through the mapping:

$$\phi_\infty \, dz = \phi_0 \, da. \tag{39}$$

Fig. 3 shows that both Eulerian and Lagrangian models converge to the Eulerian analytical solution as long as the effective stress terms remain sufficiently small. As the value of K_σ increases, a diffusion layer appears at the top of the Eulerian solution. This effect is directly related to the diffusion flux. A similar behavior is observed for sufficiently large solid volume fractions (i.e. highly concentrated suspensions).

Fig. 3(c) shows that, at very high effective stress, the diffusion layer in the Eulerian solution becomes larger than the initial height of the suspension. This behavior is similar to what is observed in highly charged colloidal suspensions in purified water (van Roij, 2003). In that case, strong electrostatic repulsion between particles leads to the formation of a diffuse (or "fuzzy") layer at the water/suspension interface. In this region, particles are no longer in contact, and the

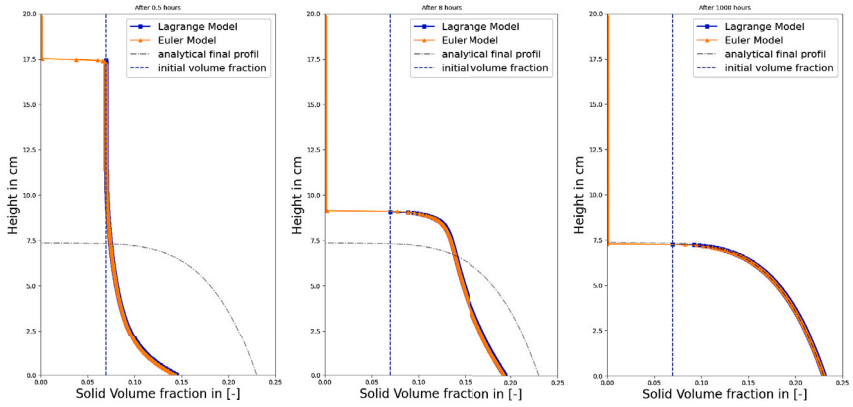

(a) Results for $n = 5.71$, $K_k = 3 \times 10^{-12}$, and $K_{\sigma 1} = 1 \times 10^{6}$.

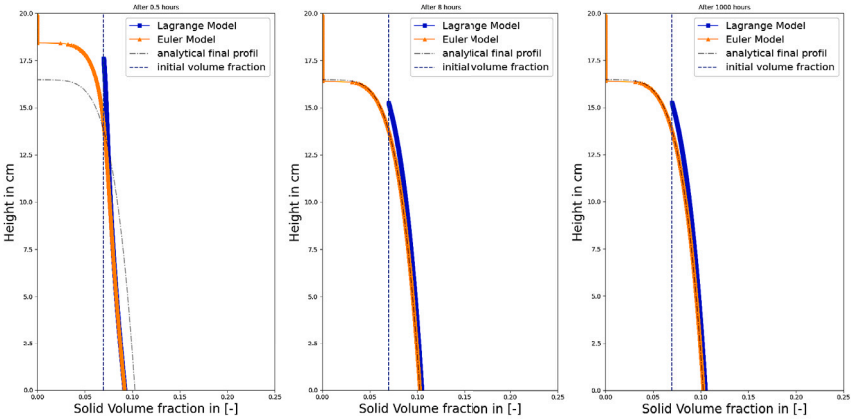

(b) Results for $n = 5.71$, $K_k = 3 \times 10^{-12}$, and $K_{\sigma 2} = 100 \times K_{\sigma 1}$.

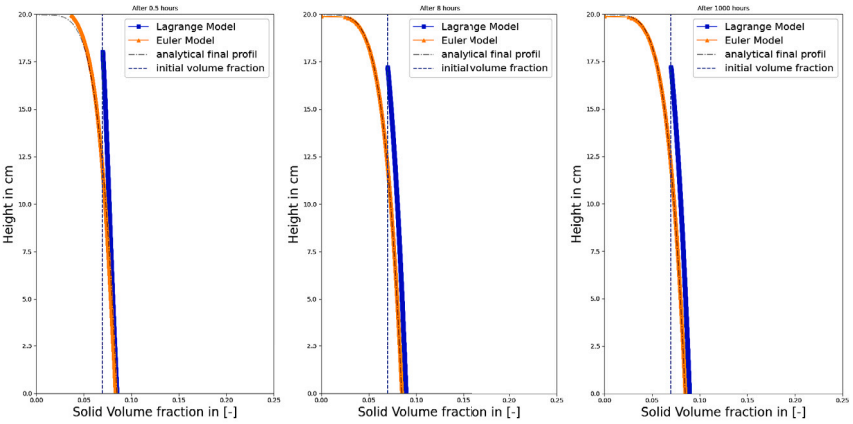

(c) Results for $n = 5.71$, $K_k = 3 \times 10^{-12}$, and $K_{\sigma 3} = 300 \times K_{\sigma 1}$.

Fig. 3. Comparison between Eulerian and Lagrangian results for different values of K_σ.

diffusion mechanism is governed by electrostatic (non-contact) interactions rather than contact forces (Chassagne, 2021). In typical soft slurry systems, where particles are larger and the water is not purified, this diffuse layer is generally not observed.

This behavior is also observed when comparing the analytical solutions at the end of consolidation, as shown in Fig. 4. The diffusion layer is present in the Eulerian analytical solution, whereas it is not observed in the Lagrangian formulation prior to mapping. This confirms that the observed diffusion is not numerical, but results from the difference in boundary conditions between the Eulerian and Lagrangian frameworks.

2.7. Benchmark testing

To check the validity of the proposed formulation, a benchmark test from Pu et al. (2018, 2020) is reproduced. This benchmark is commonly used to verify numerical models for one-dimensional large-strain consolidation based on the Gibson equation.

Problem definition. The problem considers the self-weight consolidation of a saturated soil column with an initial height $H_0 = 5$ m and an initial uniform void ratio $e_0 = 5.0$. The consolidation is driven only by gravity.

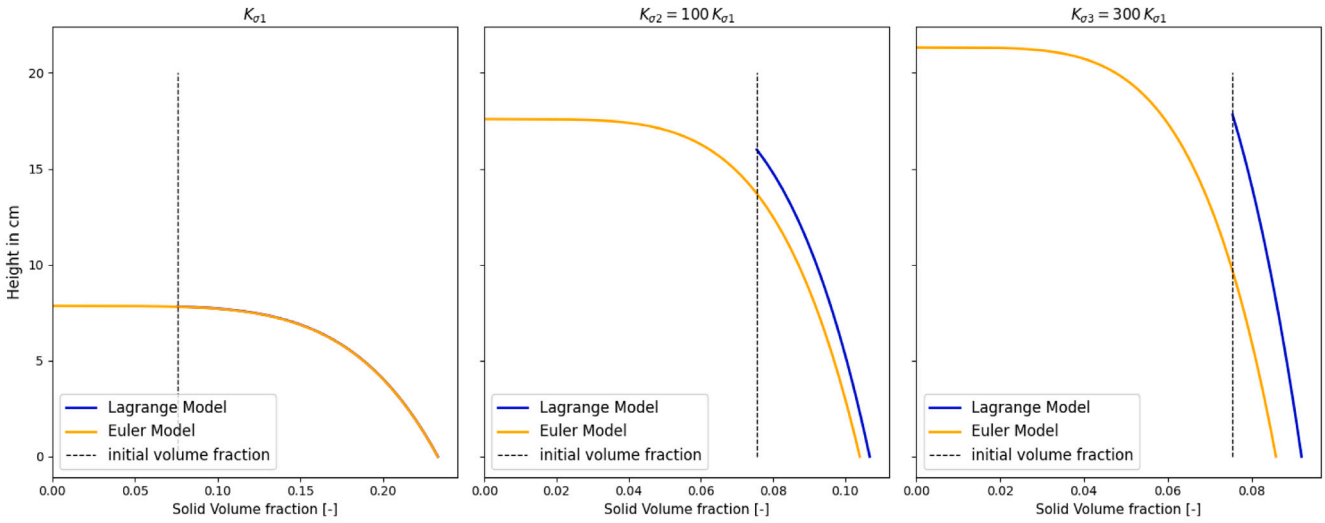

Fig. 4. Comparison between analytical profiles at the end of consolidation obtained from the Eulerian formulation and from the Lagrangian formulation after mapping, for different values of K_σ. The results show that the diffusion layer observed in the Eulerian framework is also present in the analytical solution.

Table 1
Settlement data for the single-drained benchmark case from Pu et al. (2018, 2020).

Time t (y)	Settlement S (m)
0	0.000
0.05	0.032
0.1	0.065
0.5	0.323
1	0.592
2	0.863
3	0.995
4	1.071
5	1.119
7	1.172
10	1.202
20	1.216
40	1.216

A **single-drained condition** is used: water can drain at the top, while the bottom is impermeable.

Constitutive relationships. The material behavior is defined by simple logarithmic laws linking void ratio, effective stress, and permeability rather than the fractal model used in the rest of this paper :

$$e = 5.0 - \log\left(\frac{\sigma_{sk}}{0.2\ \text{kPa}}\right), \tag{40}$$

$$e = 4.3 + 1.3\log\left(\frac{K}{2\times 10^{-8}\ \text{m/s}}\right), \tag{41}$$

These relationships are taken directly from the benchmark definition.

Numerical implementation. The problem is solved using a **one-dimensional finite difference method (FDM)** in a **Lagrangian framework**. This is the same type of approach used in classical consolidation models, which allows a fair comparison with the benchmark results.

Benchmark data for the single-drained case. For completeness, Tables 1 and 2 report the benchmark values used for the single-drained case.

Settlement comparison. Fig. 5 shows that the predicted settlement matches the benchmark very well over the whole time range. Both the rate of consolidation and the final settlement are well reproduced. This indicates that the model correctly captures the main physical mechanisms.

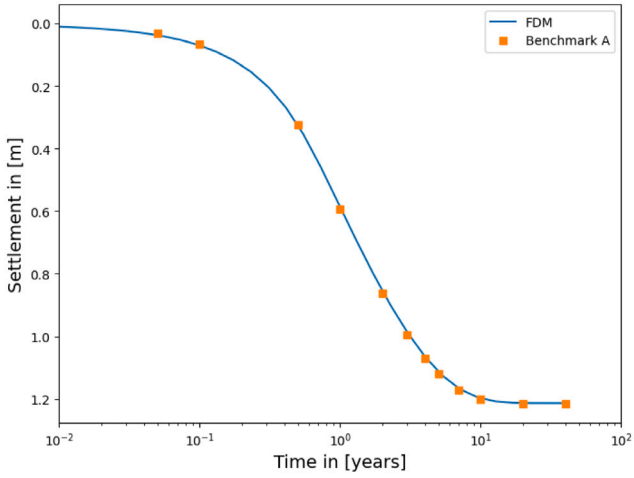

Fig. 5. Comparison of settlement over time between the present model and the benchmark solution of Pu et al. (single-drained case).

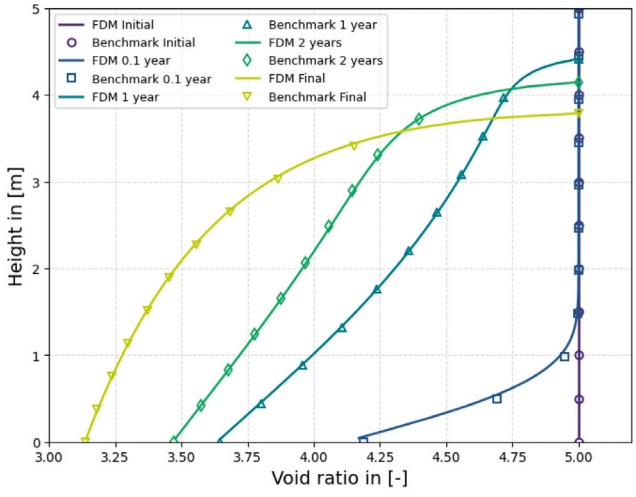

Fig. 6. Comparison of void ratio profiles at different times between the present model and the benchmark solution (single-drained case).

Table 2
Void ratio data for the single-drained benchmark case from Pu et al. (2018, 2020).

Normalized elevation Z	Initial	$t = 0.1$ year	$t = 1$ year	$t = 2$ years	Final
1.0	5.000	5.000	5.000	5.000	5.000
0.9	5.000	5.000	4.716	4.396	4.151
0.8	5.000	5.000	4.638	4.242	3.864
0.7	5.000	5.000	4.557	4.145	3.686
0.6	5.000	5.000	4.465	4.058	3.556
0.5	5.000	5.000	4.359	3.969	3.455
0.4	5.000	5.000	4.239	3.876	3.371
0.3	5.000	4.998	4.106	3.778	3.299
0.2	5.000	4.949	3.959	3.677	3.237
0.1	5.000	4.691	3.803	3.574	3.182
0.0	5.000	4.188	3.644	3.470	3.138

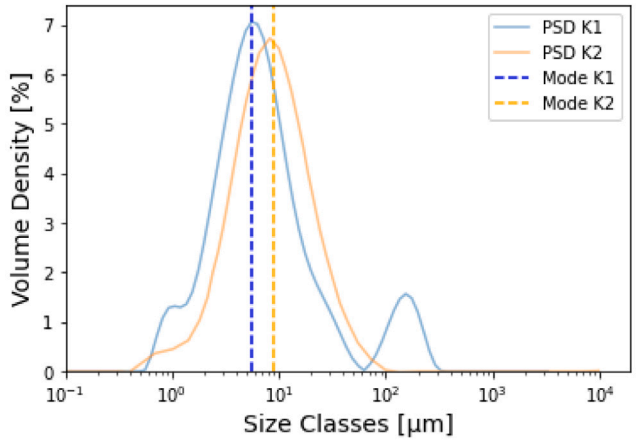

Fig. 7. Particle size distribution comparison between kaolinite K1 and K2 determined using a laser diffraction technique.

Void ratio profile comparison. Fig. 6 shows a very good agreement between the computed and benchmark void ratio profiles at all times. The model correctly reproduces the gradual densification of the soil and the non-uniform profiles that develop during consolidation.

Discussion. The good agreement for both settlement and void ratio profiles shows that the present implementation is consistent with well-established one-dimensional large-strain consolidation models, such as those of Pu et al. (2018, 2020).

This validation step is important because it confirms that the results are not affected by numerical errors, but reflect the behavior of the constitutive model itself.

3. Experimental methods

3.1. Materials

Experiments were conducted on a commercial kaolinite, Speswhite DAT002K from IMERYS Minerals Ltd, hereafter referred to as kaolinite K1. The same experiments were also performed on another kaolinite of unknown origin, referred to as kaolinite K2.

Particle size distributions of K1 and K2 suspensions were measured by laser diffraction using a Malvern 3000 particle sizer. From these measurements, median particle sizes (D_{50}) of approximately 12.50 µm and 7.79 µm were obtained for K1 and K2, respectively. Kaolinite K1 exhibits a bimodal distribution, with a first mode at 5.55 µm and a second mode around 198 µm. In contrast, kaolinite K2 shows a unimodal distribution centered around 9 µm.

The zeta potential of each clay type was measured by electrophoresis using a ZetaCompact (CAD Instruments). K2 particles in deionized water exhibit a mean zeta potential of −24.61 mV, while K1 particles show a slightly more negative value of −28.26 mV. Suspensions of different concentrations were prepared in deionized water using both kaolinites. The pH and electrical conductivity were measured (without adjustment) for each suspension (Table 3).

Table 3
Conductivity and pH values for different concentrations of kaolinite suspensions.

Type	Concentration in g/L	Conductivity in mS/cm	pH
K1	39	0.0645	5.01
K1	92	0.115	4.81
K1	185	0.192	4.72
K1	350	0.255	4.62
K1	450	0.326	4.47
K2	185	0.163	9.00

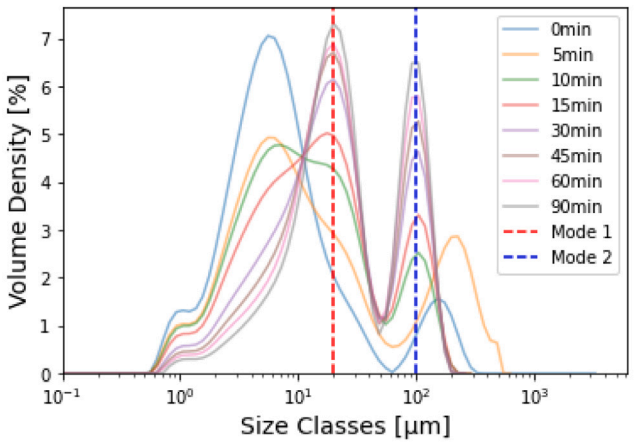

Fig. 8. Particle size distribution of kaolinite K1 at pH 4 at different times, measured using laser diffraction.

Both conductivity and pH vary with the solid concentration, indicating ion leaching from the kaolinite particles. Suspensions prepared with kaolinite K1 exhibit acidic conditions, whereas K2 suspensions are basic. The electrical conductivity is not significantly different between K1 and K2 for similar particle concentrations.

To investigate the effect of acidic conditions caused by leaching on the particle size distribution of kaolinite K1, additional laser diffraction measurements were performed on K1 suspended in deionized water adjusted to pH 4 using HCl. Fig. 8 shows the particle size distributions recorded at different times.

Over time, the data show a clear evolution of the distribution. The initial peak at 5.55 µm decreases, while a new peak (Mode 1, around 25 µm) progressively develops and becomes dominant after approximately 15 min. At the same time, the initial peak at 198 µm shifts toward a second mode (Mode 2) centered around 100 µm. The appearance of these two modes indicates that flocculation processes are occurring.

Importantly, these results show that flocculation kinetics are very fast, on the order of minutes. This observation will be relevant for the interpretation of the settling column experiments.

4. Methods

In this study, Nuclear Magnetic Resonance (NMR) is used as a non-destructive technique to measure water content profiles during sedimentation. NMR exploits the magnetic properties of nuclei possessing a magnetic moment, such as hydrogen (^{1}H). When placed in

a static external magnetic field B_0, the magnetic moments precess at the Larmor frequency:

$$\omega_0 = \gamma B_0, \tag{42}$$

where γ is the gyromagnetic ratio (for ^{1}H, $\gamma = 42.58$ MHz/T), and B_0 is the magnitude of the static magnetic field.

By applying an oscillating radio-frequency (RF) field at the Larmor frequency, the magnetic moments can be manipulated. Using pulsed sequences such as the Hahn spin-echo or Carr–Purcell–Meiboom–Gill (CPMG) sequence, spin-echo signals are generated. The amplitude of these signals is proportional to the density of hydrogen nuclei and therefore directly related to the local water content. The measured NMR signal S can be expressed as Meiboom and Gill (1958):

$$S \propto \rho \left(1 - e^{-TR/T_1}\right) e^{-TE/T_2}, \tag{43}$$

where ρ is the density of hydrogen nuclei, T_1 is the spin-lattice (longitudinal) relaxation time, TR is the repetition time, T_2 is the spin–spin (transverse) relaxation time, and TE is the spin-echo time.

To minimize T_1-weighting effects, the repetition time is typically chosen such that $TR > 4T_1$. As a result, the measurement time is governed by the longest T_1 present in the system. In sedimentation experiments, this corresponds to the free water phase, where $T_1 \approx 3$ s, leading to repetition times on the order of 10–12 s.

To overcome this limitation, a multi-slice stepper motor method is employed (N.J. Hol et al., 2025). In this approach, the sample column is translated through the NMR setup and measurements at different spatial positions are interleaved. This allows optimal use of the repetition time while maintaining high spatial and temporal resolution, effectively reducing the total acquisition time compared to conventional single-slice measurements. By combining spin-echo signals acquired at different positions, one-dimensional moisture profiles are obtained.

In addition to the signal amplitude, the decay of the spin-echo signal provides information on the transverse relaxation time T_2, which is sensitive to the local microstructure. In sediment systems, T_2 relaxation is strongly influenced by interactions between water molecules and solid particle surfaces. As water molecules diffuse during an NMR experiment, they probe the pore space (Brownstein and Tarr, 1979). As sedimentation and consolidation proceed, the pore structure evolves, which is reflected in changes in T_2.

For porous media, the transverse relaxation time can be related to the pore geometry through (Valckenborg et al., 2001):

$$\frac{1}{T_2} = \rho_2 \frac{S}{V}, \tag{44}$$

where ρ_2 is the surface relaxivity, S is the pore surface area, and V is the pore volume. This relationship shows that T_2 is proportional to the pore volume-to-surface ratio (V/S), which represents a characteristic pore size.

For idealized spherical pores, this simplifies to:

$$T_2 \propto r, \tag{45}$$

where r is the pore radius. Consequently, the pore size distribution can be inferred from the measured T_2 distribution and the determined surface relaxivity for a given sediment (N. Hol et al., 2025).

All experiments in this study were performed using a small-scale one-dimensional NMR scanner operating at a static magnetic field of 0.78 T with a static gradient of ±0.1 T/m. The spin-echo time was set to $TE = 300$ µs, and a CPMG sequence with 2048 pulses was used. The sedimentation column had a diameter of 23 mm and a length of 200 mm, containing approximately 80 mL of suspension. The NMR system was equipped with a Faraday shield to ensure quantitative measurements (Kopinga and Pel, 1994; Pel et al., 2016).

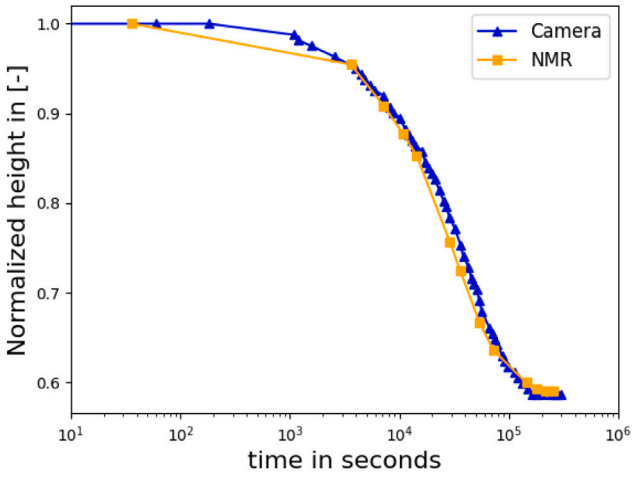

Fig. 9. Water/suspension interface as a function of time, measured using NMR (orange) and a camera (blue). In both cases, a 185 g/L kaolinite K1 suspension was used in similar settling columns.

Table 4
Examples of calibrated parameter sets (D_f, K_σ, K_k) providing similar agreement with the experimental density profile and interface evolution.

D_f	K_σ (Pa)	K_k (m/s)
2.65	9.00×10^6	3.0×10^{-12}
2.66	1.42×10^7	1.7×10^{-12}
2.67	2.70×10^7	1.1×10^{-12}
2.68	3.00×10^7	7.0×10^{-13}
2.69	5.00×10^7	4.0×10^{-13}
2.70	7.50×10^7	2.3×10^{-13}
2.00	6.20×10^3	4.2×10^{-8}

5. Results and discussions

5.1. Scanning speed verification

To verify that the NMR scanning speed is sufficient to capture the consolidation process, the water/suspension interface of two identical suspensions in similar settling columns was monitored: one using NMR and the other using a high-resolution camera (see Fig. 9). The results show that the interface evolutions overlap, in agreement with the findings of N.J. Hol et al. (2025).

5.2. Profile at the end of consolidation

The density profile at the end of consolidation for kaolinite K1 with a concentration of $C = 350$ g/L, obtained from NMR experiments, is shown in Fig. 10. In principle, one could expect a unique set of parameters (D_f, K_σ) when fitting the data using Eqs. (34), (35), (36).

To investigate this, several values of D_f were tested, while recalibrating the associated parameters K_σ and K_k for each case.

The results shown in Fig. 11 indicate that both the interface evolution and the final density profile are reproduced with a similar level of accuracy over a narrow range of D_f values, provided that K_σ and K_k are adjusted accordingly. Small values of D_f do not reproduce the parabolic shape of the NMR data, although the interface evolution is still well captured.

The corresponding calibrated parameter sets are summarized in Table 4. A clear trend is observed: as D_f increases, K_σ increases while K_k decreases. This indicates that changes in D_f can be compensated by adjustments in the other parameters, leading to comparable model predictions.

These results indicate that D_f is not uniquely identifiable from the present dataset. The model response mainly depends on the balance

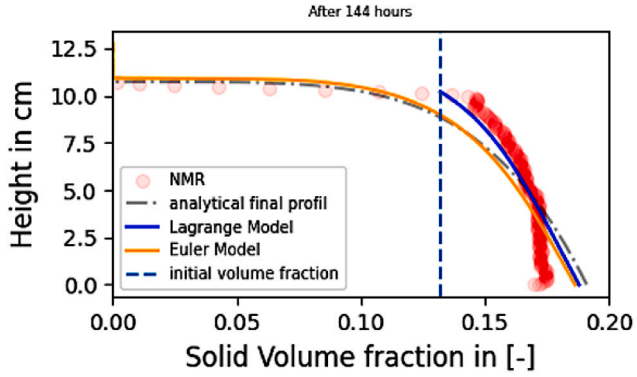

(a) Comparison between NMR profile and the standard model in both Eulerian and Lagrangian formulations.

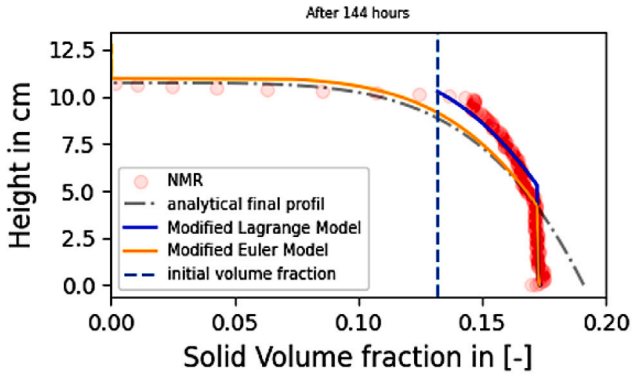

(b) Comparison between NMR profile and the modified model accounting for maximum compaction.

Fig. 10. Comparison between NMR results and numerical modeling at the end of consolidation for a kaolinite K1 suspension with a concentration of 350 g/L.

between advective and diffusive flux contributions, rather than on the value of D_f alone. For this reason, $D_f = 2.65$ is selected as a reference value for the remainder of this study.

Using this fixed value, the results are shown in Fig. 10(a), and the corresponding parameters are listed in Table 2. A first observation is that the Eulerian Gibson formulation does not accurately reproduce the density profile for solid volume fractions above the initial value. In contrast, the Lagrangian formulation provides better agreement with the experimental data.

A second observation is that the NMR results show that the solid volume fraction reaches a maximum value $\phi_{\max}$ at the bottom of the column. This behavior is not captured by the classical Gibson–Merckelbach formulation in either the Eulerian or Lagrangian framework, highlighting a limitation of the model in highly compacted regimes.

In the standard Gibson–Merckelbach formulation, the soil is assumed to have unlimited compaction capacity, meaning that the solid volume fraction can reach unphysical values greater than 1 if the stress conditions allow it. In reality, especially for incompressible particles, the solid volume fraction remains well below 1. For rigid spherical particles, for example, the maximum packing fraction is approximately 0.74.

To reproduce this behavior, a modification of the permeability is introduced. In the present formulation, both advective and diffusive fluxes are proportional to the permeability. As a result, when the permeability tends to zero, the fluid fluxes also vanish. Since consolidation

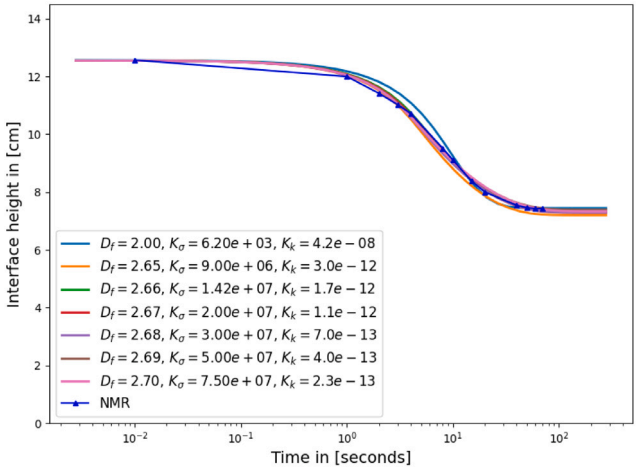

(a) Interface evolution for different values of D_f with calibrated parameters.

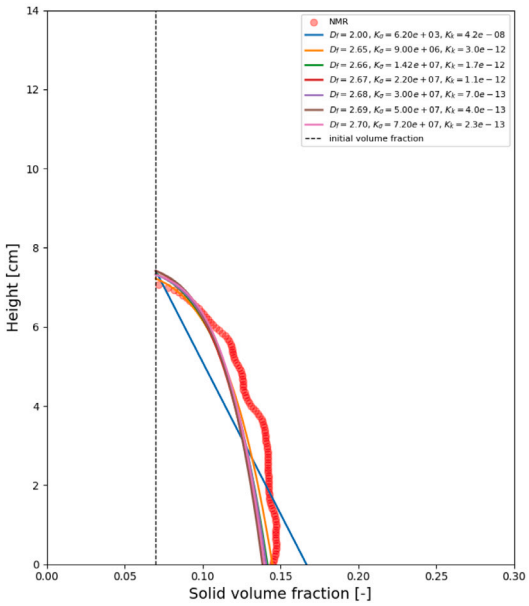

(b) Final solid volume fraction profiles compared with NMR data.

Fig. 11. Sensitivity of the model response to the choice of fractal dimension D_f. Similar agreement with experimental data is obtained for different values of D_f by adjusting K_σ and K_k, indicating that D_f is not uniquely identifiable.

is driven by fluid flow, this naturally limits further densification and leads to a maximum solid volume fraction.

This is implemented in the numerical model by multiplying the permeability by a sigmoid-type function that tends to zero as the solid volume fraction approaches the maximum compaction value (see Appendix B).

It is important to note that, in reality, reaching such a state would also affect the effective stress and compressibility. However, modeling this effect would require characterizing the effective stress behavior in highly compacted regimes, which is not directly accessible from the available experimental data. For this reason, the modification is limited to the permeability, while the effective stress relation is kept unchanged.

The modified Gibson–Merckelbach model is applied to the NMR profile of kaolinite K1 at a concentration of 350 g/L at the end of consolidation, and the result is shown in Fig. 10(b). The parameter α is

Table 5
Calibrated parameters for the modified Gibson model used to simulate consolidation for different concentrations of kaolinite K1.

Type	Concentration in g/L	D_f	K_σ	K_k	$\phi_{\max}$	α
K1	450	2.65	3.5e+06	3.8e−12	0.185	2000
K1	350	2.65	3.5e+06	3.8e−12	0.171	2000
K1	185	2.65	9.0e+06	3e−12	0.135	2000
K1	92	2.65	9.0e+06	3e−12	0.121	2000
K1	39	2.65	9.0e+06	3e−12	0.115	2000

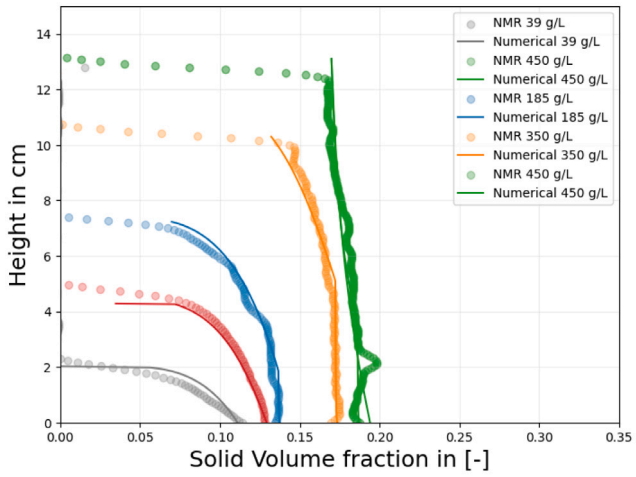

Fig. 12. Final solid volume fraction profiles for different concentrations, with corresponding model fits.

set to 2000 and $\phi_{\max}$ is set to 0.171. The results show that the modified Lagrangian Gibson model provides a better fit to the experimental data [Fig. 12].

5.3. Time evolution of the density profile

The modified Gibson model has been adopted to model all measured concentrations. It was found that using the Lagrange frame the theory and experimental data overlap quite well except for the very diluted suspensions. In this case, for C = 39 g/L, see Fig. 17, using the Euler frame enables to capture the sharp change in density observed at the water/slurry interface. This density gradient is attributed to the structure of the formed clayey matrix. Downwards into the column, the particles experience more and more load from particles above them. At the water/slurry interface, the first layer of particles can have a very loose structure, while the one below contains particles that are already more confined, hence the sharp change in density. The Euler frame also exhibits better numerical stability in the small particle concentration range. The results are shown in Figs. 13, 14, 15, 16 and 17. The set of parameters that have been used are summarized in Table 5. The density profiles found by NMR for the lowest clay concentrations are peculiar, exhibiting regions of space where the density decreases as function of depth (for instance, see in Fig. 16 the profile at 5 h after start), whereas the opposite would be expected. This was attributed to the complex hydrodynamics occurring in the settling tube (Guazzelli and Morris, 2011), triggered by the significant electrical attraction between particles at this low pH, which leads to the flocculation shown in Fig. 8.

5.4. Influence of pH and ionic concentration

For clay concentrations below 185 g/L, a different set of K_k and K_σ had to be used to fit the data compared to higher concentrations. At the same time, the maximum compaction parameter ϕ_{max} was observed to increase with the initial concentration. This variation is correlated with an increase in electrical conductivity with clay concentration (see Fig. 18), due to ion leaching when the kaolinite clay is dispersed in purified water.

As more ions are leached, electrostatic interactions between the kaolinite particles are reduced, which may promote a more compact stacking of the platelets. These interactions influence both permeability (and hence K_k) and compressibility (and hence K_σ). These observations are consistent with recent studies investigating the effect of pore-fluid salinity on kaolinite behavior (Tafili et al., 2026), which show that increasing ionic strength influences compressibility and soil structure. In the present work, this influence is captured indirectly through calibrated macroscopic parameters.

In Fig. 19, the final profiles of K1 and K2 suspensions with the same initial concentration of $C = 185$ g/L are shown. Since the pH is basic for the K2 suspension, face-to-face aggregation is commonly reported in this case (Lagaly and Dékány, 2013). On the other hand, the pH is acidic for the K1 suspension, for which edge-to-face aggregation is often observed, as the edges of the kaolinite particles are positively charged while their faces are negatively charged, leading to Coulombic attraction.

The edge-to-face configuration (“house of cards” structure) is generally associated with a more open structure, whereas the face-to-face configuration corresponds to a more compact arrangement, as illustrated in Fig. 20. This interpretation is consistent with the observed difference in maximum compaction, where $\phi_{max} = 0.185$ for K2 is larger than $\phi_{max} = 0.135$ for K1.

It is important to note that the present model does not explicitly incorporate electrochemical interactions at the particle scale. Instead, the influence of pH and ionic strength is captured indirectly through the calibrated macroscopic parameters (K_σ, K_k, and ϕ_{max}). Consequently, the relationship between electrochemical conditions and model parameters should be interpreted as empirical rather than mechanistic.

While clear qualitative trends are observed (e.g., an increase in ϕ_{max} with increasing conductivity), the proposed microstructural interpretations remain indirect and are not directly demonstrated by the NMR measurements. A direct quantitative coupling would require a more detailed physico-chemical model, which is beyond the scope of the present study.

5.5. End profile of pore size distribution

The differences in ϕ_{max} observed for the K1 and K2 suspensions are also reflected in differences in pore sizes. At the position in the column where $\phi_s = \phi_{max}$, the mean pore size for the K1 suspension is found to be 2.64 μm, which is larger than that of the K2 suspension, measured at 2.40 μm (see Fig. 19). As illustrated in Fig. 2, the model described in Section 2.5 assumes that the size of the largest pores in the system scales with $R_N(z)$.

A value of $R_0 = 5.70$ μm was used for both K1 and K2 suspensions. This value is close to $R_0 = 5.55$ μm, obtained from NMR measurements at the initial homogeneous state, which also corresponds to the first mode of the particle size distribution (see Fig. 7).

It is observed that the model underestimates the pore size compared to the NMR measurements, as shown in Fig. 21.

When the parameter set corresponding to $D_f = 2.65$, $K_\sigma = 9 \times 10^6$, and $K_k = 3.0 \times 10^{-12}$ is used, the model underestimates the pore size but captures the overall trend of the profile. As discussed previously (see Fig. 21), multiple parameter sets can fit the experimental interface data. Based on the pore size relation, selecting a different value of D_f can improve the pore size prediction.

It is found that choosing $D_f = 2.00$ provides a better overall agreement with the pore size measurements (see Fig. 22). The corresponding parameters used to fit the final height and the interface evolution are $K_\sigma = 6.2 \times 10^3$ and $K_k = 4.5 \times 10^{-8}$.

The very low value of D_f gives the final solid volume fraction profile a more linear trend and does not fit as well as higher values

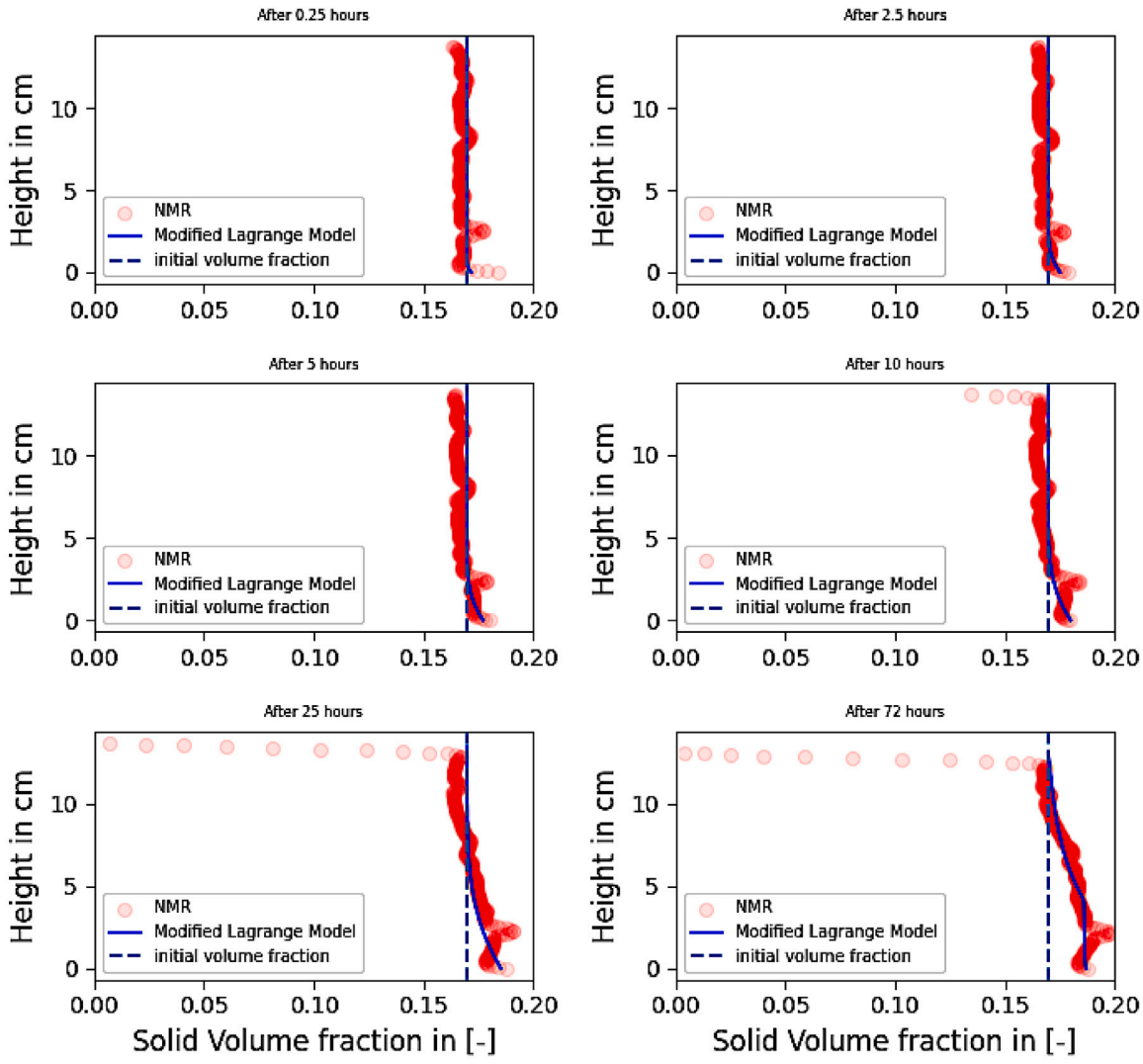

Fig. 13. Solid volume fraction profiles for K1 suspension of a concentration of 450 g/L in different times.

of D_f (see Figs. 11(a) and 11(b)). This mismatch between theory and experimental data can be explained by the assumption that the pore structure follows a perfect fractal behavior. Although this assumption is useful and explains the exponential form of the constitutive model for normally consolidated soils, it is not fully accurate.

5.6. Interface as a function of time

The model predicts the interface evolution as a function of time for most cases, except at low concentrations (see in particular Figs. 16 and 17). This is because there is a critical initial clay concentration above which particles are, from the start, in the consolidation regime. Below this critical concentration, called the "gelling concentration", particles at the water/slurry interface undergo settling for some time.

As discussed in Section 2, the model assumes that settling and consolidation can be described within a single continuous framework, provided that a continuous particle network is formed. However, this assumption relies on the existence of such a network, which allows the definition of an effective stress and a consolidation process driven by pore water pressure dissipation.

For dilute suspensions, this condition is not satisfied. Particles are not in continuous contact, and no effective stress can be defined. In this regime, settlement is governed by hindered settling, where particle motion results from the balance between gravity and hydrodynamic drag, rather than pore pressure dissipation.

As a consequence, the diffusive term in the model, which represents inter-particle contact forces, loses its physical meaning. This explains why a separate description is required below the gelling concentration.

At low clay concentrations, there is a discontinuity between the settling and consolidation regimes. This is visible in Fig. 24, where the change of regime is indicated by a black dot. At low clay concentrations, the settling velocity of the interface can be modeled using the well-known Richardson and Zaki expression:

$$v = v_0(1 - \phi_s/\phi_{gel})^m \tag{46}$$

where v_0 is the Stokes settling velocity (m/s), ϕ_s is the concentration of the settling phase (equal to the initial concentration, i.e. $\phi_s = \phi_0$), and m is an adjustable parameter. The coefficient m is typically larger than 5 for non-spherical particles (Dietrich, 1982). The gelling concentration ϕ_{gel} is defined as the average concentration of the slurry at the time

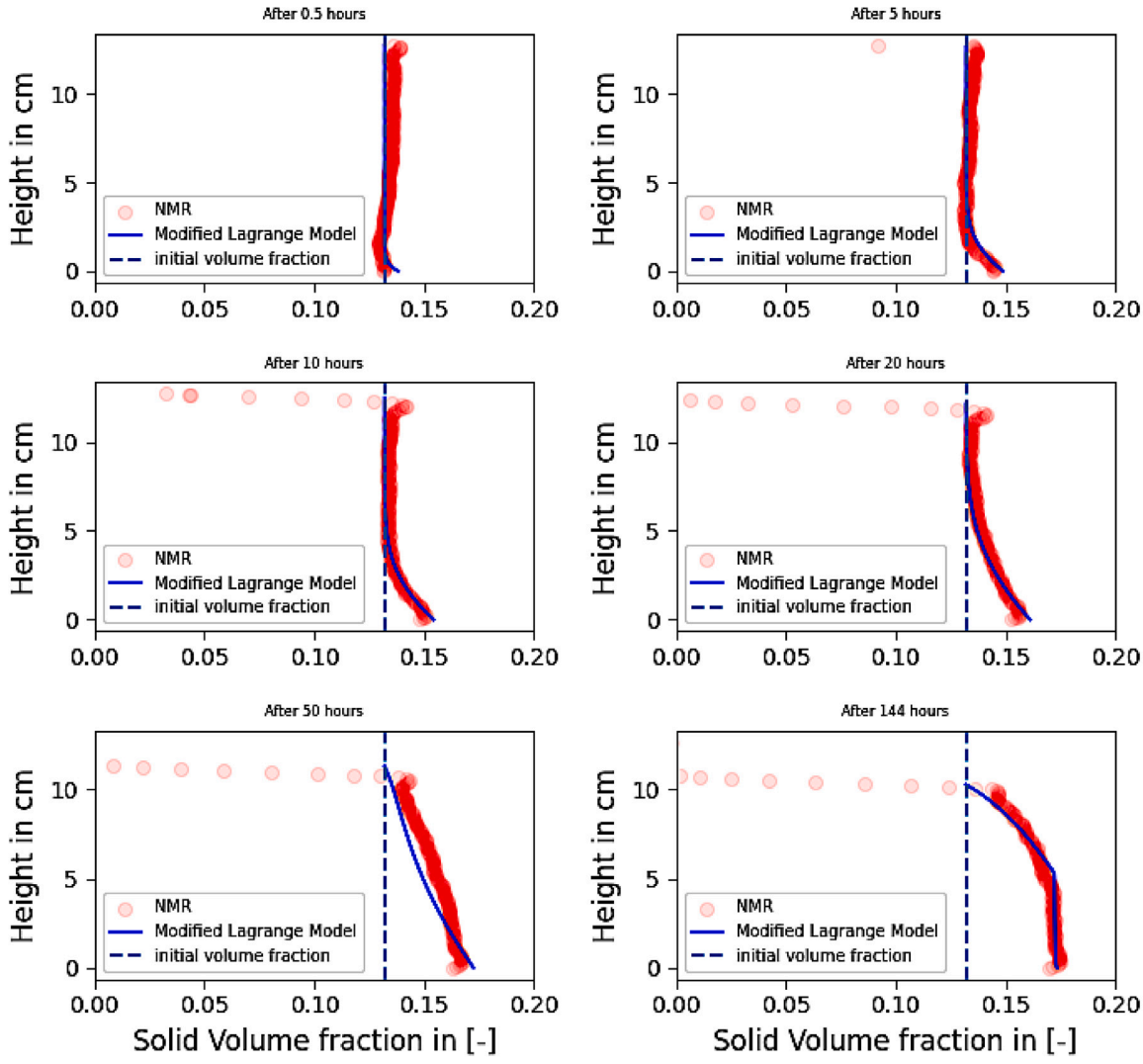

Fig. 14. Solid volume fraction profiles for K1 suspension of a concentration of 350 g/L at different times.

when the settling phase disappears and all particles in the column are in direct contact.

By fitting the interface as a function of time at early times (when the curve is approximately linear), a hindered settling velocity of 4 μm/s is obtained (see Fig. 23). This is illustrated by the blue line in the figure. The second fit, shown by the green line, corresponds to the linear fit just after the gelling point is reached. The gelling time is determined from the intersection of the two linear fits and is found to be about 5 h. The gelling concentration is then calculated by mass balance:

$$\phi_0 H_0 = \phi_{gel} H_{gel} \tag{47}$$

where H is the water/slurry height. The value of ϕ_{gel} is found to be 0.072, corresponding to 190 g/L. This estimation remains approximate and depends on the selected fitting ranges. It is expected to be more reliable when density variations during the transition are limited. In larger columns, where stronger spatial gradients may develop, this approach may become less accurate.

The estimated value of 190 g/L is close to the 185 g/L sample. This suggests that the latter lies near the transition between sedimentation and consolidation and may therefore exhibit a short initial sedimentation phase. This observation should be interpreted with caution due to the uncertainty associated with the estimation method.

This interpretation is consistent with the observation that the consolidation behavior of the 185 g/L sample can be described over the full time range using the Gibson model, indicating that its initial volume fraction is close to, or slightly above, the gelling concentration. The Stokes velocity can be estimated using:

$$v_0 = \frac{(\rho_s - \rho_w) g d^2}{18\mu} \tag{48}$$

where μ is the dynamic viscosity of the fluid, d is the particle diameter, ρ_s is the solid density, and ρ_w is the water density. Using the particle size from Fig. 5 for mode 1 (i.e. 25 μm), corresponding to the size of the settling particles at the water/slurry interface (larger particles from mode 2 settle faster), a Stokes settling velocity of 5.4×10^{-4} m/s is obtained. The adjustable parameter m can then be evaluated from Eqs. (46) and (48). The value of m is estimated to be 7.37, which is within the typical range for anisotropic particles. Note that, due to flocculation (see Fig. 24), the measured settling rate increases over time compared to the predicted value.

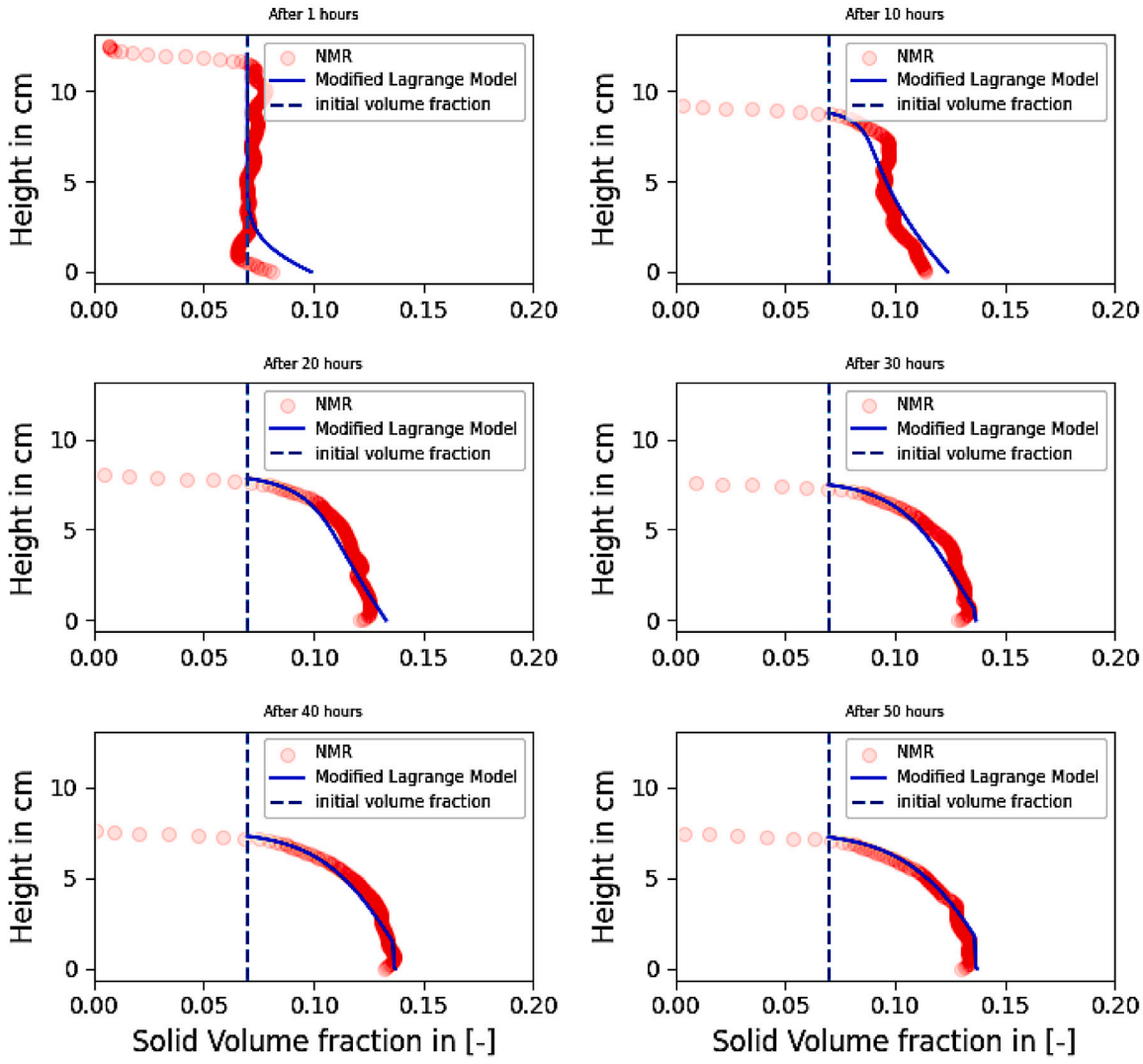

Fig. 15. Solid volume fraction profiles for K1 suspension of a concentration of 185 g/L at different times.

6. Conclusion

In this study, the consolidation behavior of kaolinite suspensions under different electrochemical conditions was investigated using a combined experimental–numerical approach based on Nuclear Magnetic Resonance (NMR) measurements and large-strain consolidation modeling.

The results show that classical large-strain formulations based on the Gibson equation can capture the general evolution of density profiles and interface positions. The comparison between Eulerian and Lagrangian formulations indicates that the main differences arise from boundary conditions and problem formulation. In particular, the Eulerian formulation leads to the appearance of a diffusion layer at the water/bed interface at high concentrations, which is not observed experimentally. In such cases, the Lagrangian formulation provides a more consistent description.

A key result of this work is that NMR measurements reveal the existence of a maximum solid volume fraction at the bottom of the column, which cannot be reproduced by the Gibson–Merckelbach framework. This highlights a limitation of standard large-strain consolidation models when combined with the fractal constitutive model of Merckelbach and Kranenburg (2002) in highly compacted regimes. A simple modification based on a reduction of permeability was introduced to reproduce this behavior. This modification can be interpreted as a hydraulic limitation of the model.

The comparison between model predictions and NMR measurements also shows that the model captures the main trends of the pore size distribution. However, discrepancies remain in magnitude, and the agreement depends on the calibration of the model parameters, reflecting limitations of the current constitutive assumptions.

Finally, the results indicate that, for dilute suspensions, the assumption that a single constitutive framework can describe both settling and consolidation is not fully valid. A transition occurs at the gelling point, below which particle settling is better described using hindered settling formulations. Beyond this transition, the model remains able to capture the evolution of density profiles and interface positions.

Overall, this work provides insight into both the capabilities and limitations of large strain Gibson–Merckelbach consolidation models when compared with high-resolution experimental data.

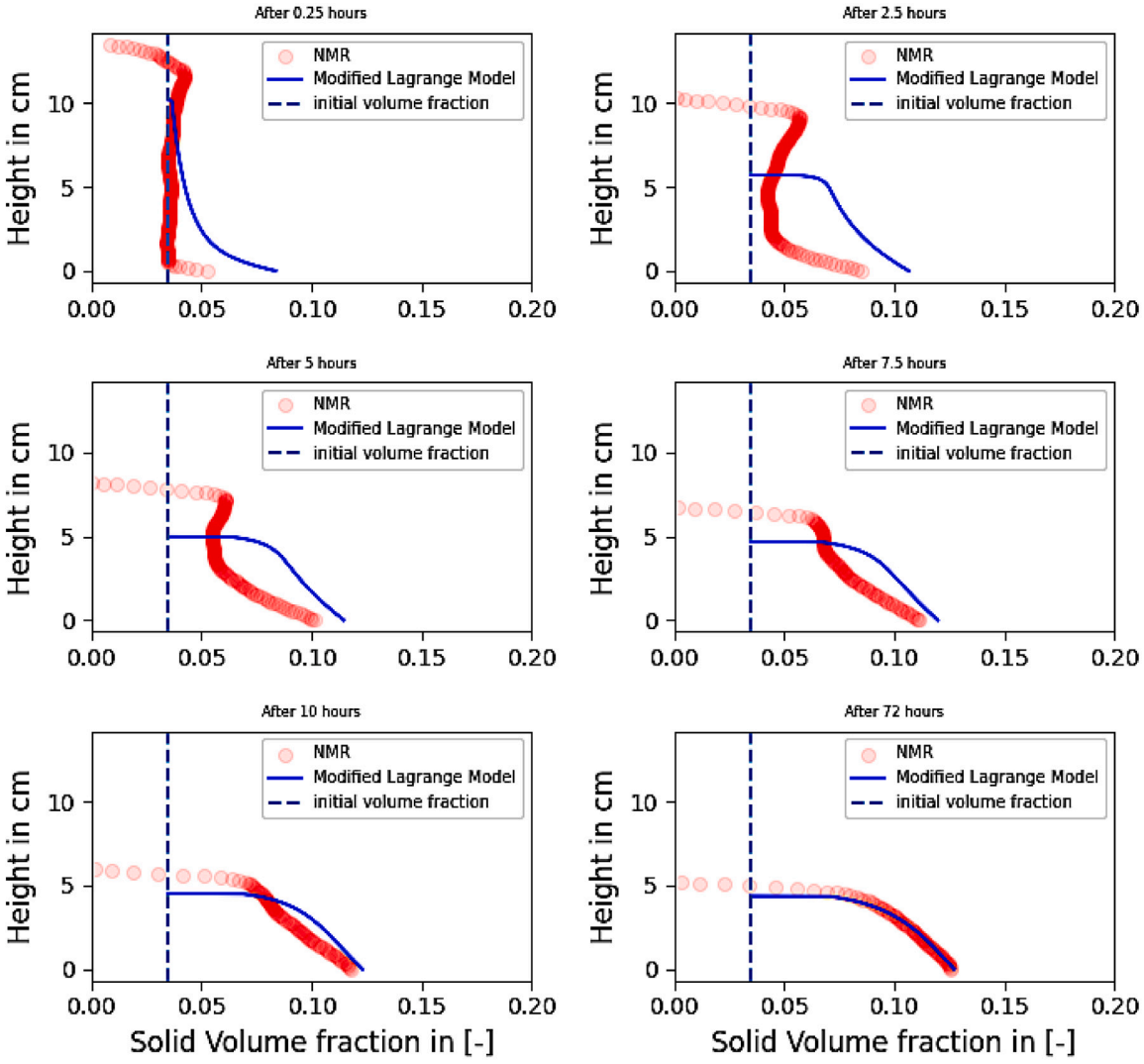

Fig. 16. Solid volume fraction profiles for K1 suspension of a concentration of 92 g/L at different times.

CRediT authorship contribution statement

Ismail Myouri: Writing – review & editing, Writing – original draft, Visualization, Validation, Software, Methodology, Investigation, Formal analysis, Data curation, Conceptualization. **Nick Hol:** Writing – review & editing, Visualization, Validation, Methodology, Investigation, Formal analysis, Data curation, Conceptualization. **Leo Pel:** Writing – review & editing, Supervision, Resources, Formal analysis, Data curation. **Claire Chassagne:** Writing – review & editing, Supervision, Resources, Conceptualization.

Funding declaration

This work was carried out within the Sediment-to-Soil (S2S) project and was supported by the Dutch Research Council (NWO), Netherlands under the Open Technology Programme, grant number 2020-II TTW (2021/TTW/01144385). The Sediment-to-Soil project is part of MUDNET, the academic network for research on fine-grained sediments.

Declaration of competing interest

The authors declare that they have no known competing financial interests or personal relationships that could have appeared to influence the work reported in this paper.

Acknowledgment

The authors express their gratitude to Dr. Angela Casarella (Chalmers University of Technology, Göteborg, Sweden) for her insightful discussions on given insight on the microstructural behavior of clay kaolinite. They also thank the TU Delft MUDNET community for their support and the productive sparring sessions throughout the project.

Appendix A

A.1. Lagrange frame and material coordinates

The Gibson equation presented in the main body of the article was expressed in the Eulerian frame of reference. An alternative way to write this equation is in the Lagrange frame of reference, i.e. a time-dependent coordinate system that moves with the solid particles. Using material coordinates is interesting because it affects the formulation of the necessary boundary conditions at the top and bottom of the settling column. Also, a defined elementary volume at time $t = 0$ will always, by definition, contain the same volume of solid particles at any time t (see Fig. 25). This feature of the model will be useful for further studies where (bio)chemical reactions will be included in the consolidation model.

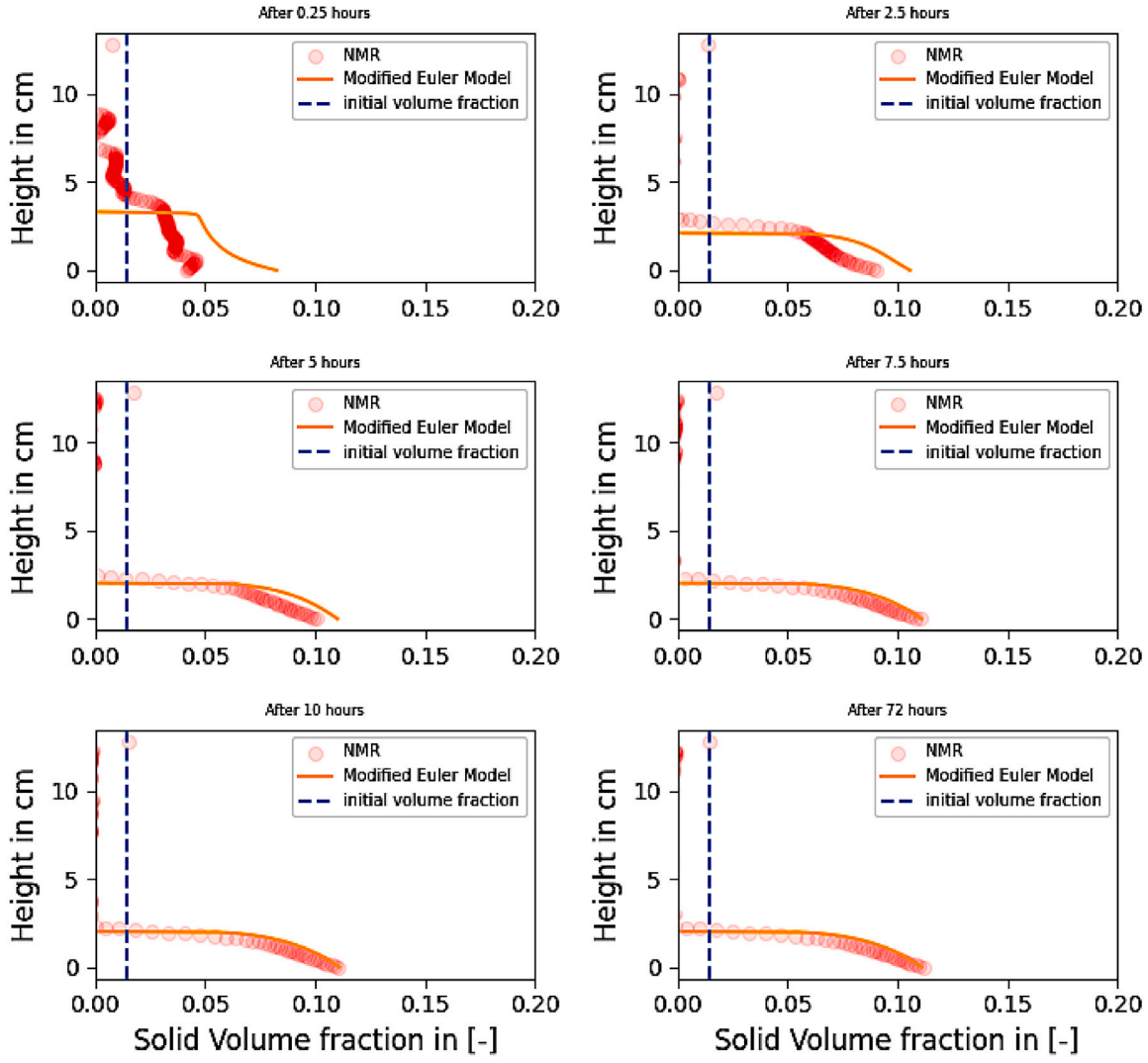

Fig. 17. Solid volume fraction profiles for K1 suspension of a concentration of 39 g/L at different times.

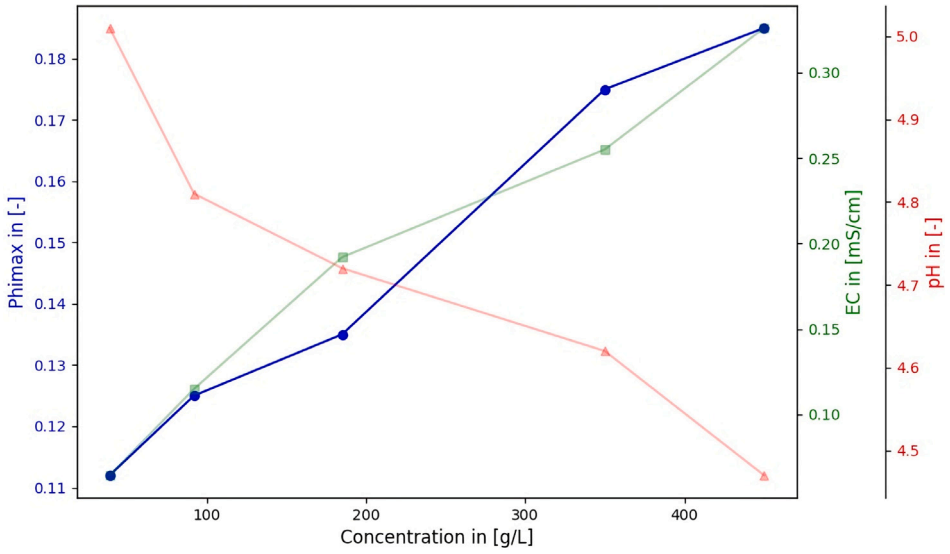

Fig. 18. Variation of electrochemical conditions and maximum compaction with the initial concentration.

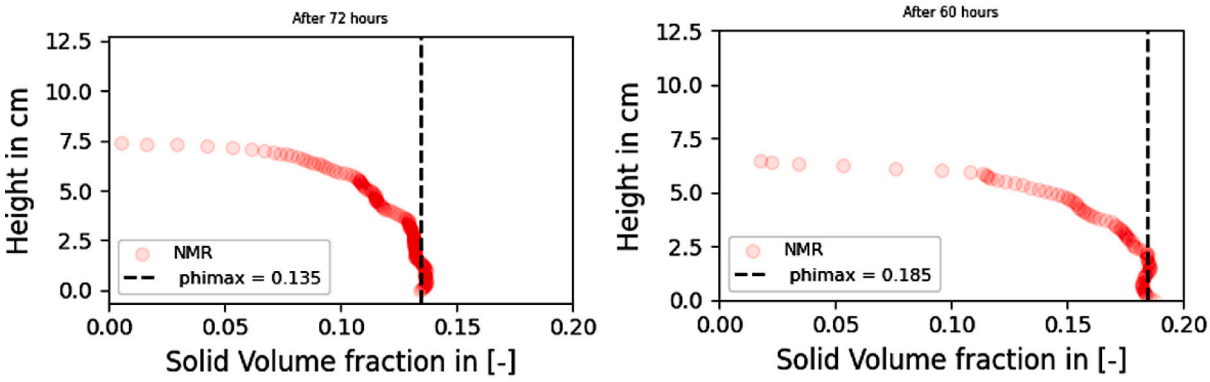

(a) Kaolinite K1 (b) Kaolinite K2

Fig. 19. Solid volume fraction profiles of kaolinites K1 and K2 at the end of consolidation for the same concentration of 185 g/L.

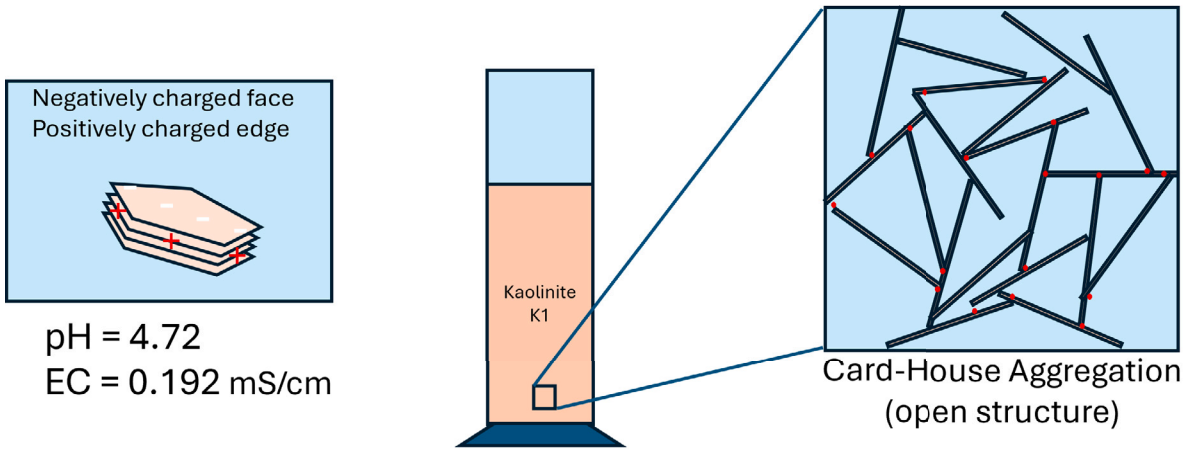

(a) Kaolinite K1

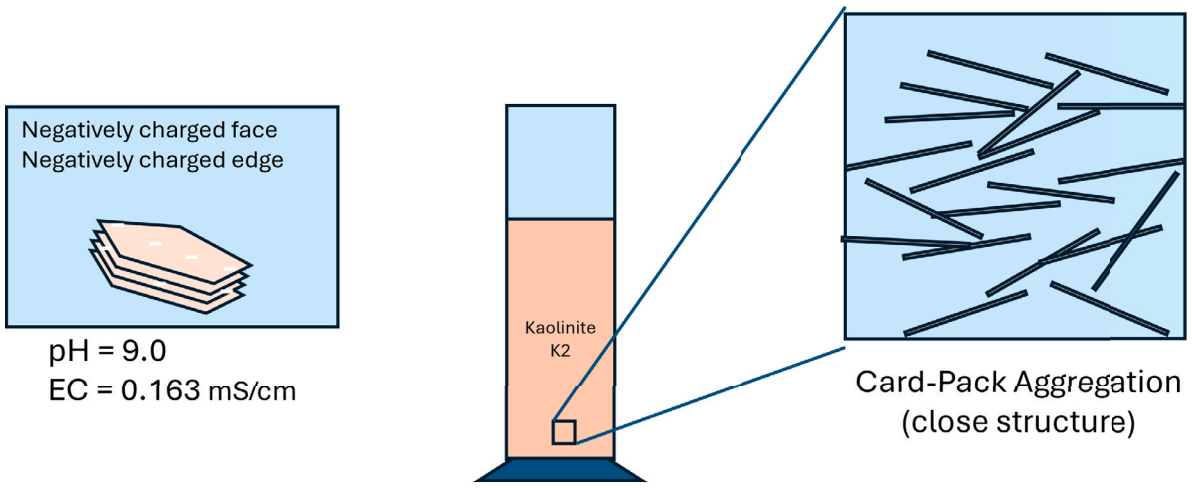

(b) Kaolinite K2

Fig. 20. Conceptual schematic illustrating possible particle arrangements of kaolinite K1 and K2 under different electrochemical conditions. These configurations are proposed as interpretations based on literature and indirect experimental evidence.

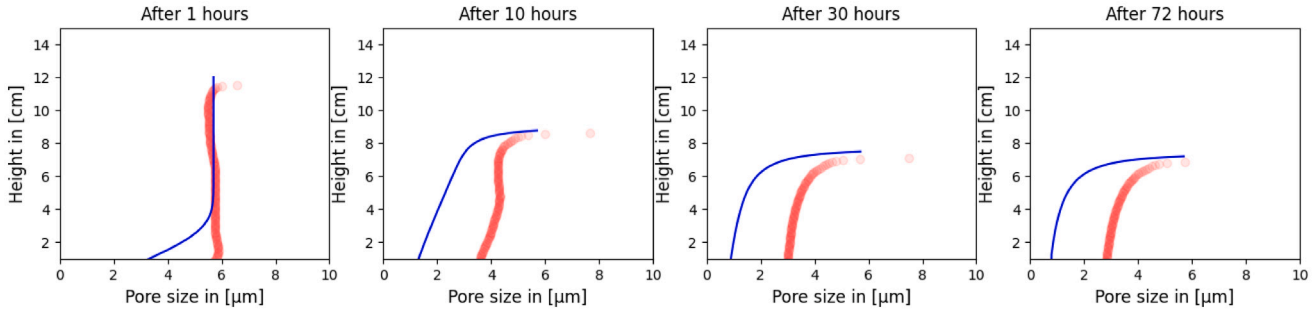

Fig. 21. Model prediction of pore size based on Merckelbach theory compared to NMR measurements, for $D_f = 2.65$, $K_\sigma = 9 \times 10^6$, and $K_k = 3.0 \times 10^{-12}$.

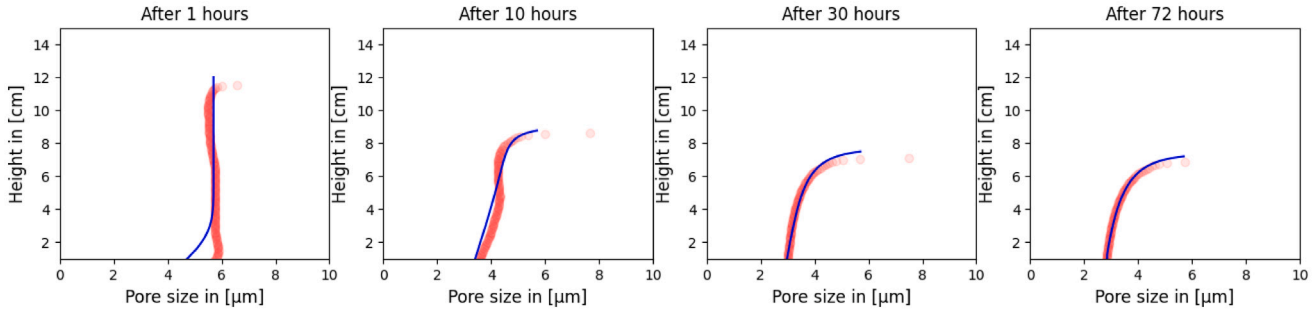

Fig. 22. Model prediction of pore size based on Merckelbach theory compared to NMR measurements, for $D_f = 2.00$, $K_\sigma = 6.2 \times 10^3$, and $K_k = 4.5 \times 10^{-8}$.

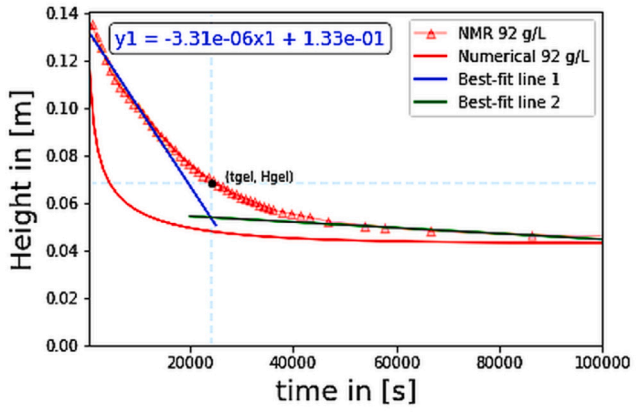

Fig. 23. Linear fitting of the settlement profiles of kaolinite K1 for a 92 g/L suspension, used to determine the gelling point.

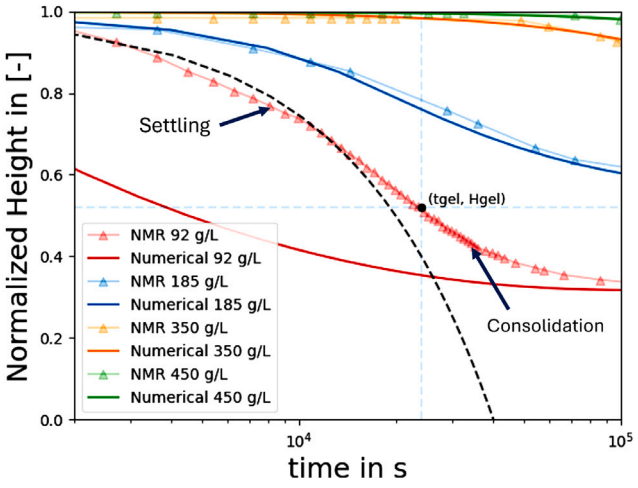

Fig. 24. Numerical fitting of the settlement profiles of kaolinite K1 measured by NMR using the calibration parameters from Table 5.

Based on that, a material coordinate variable z_{vol} is defined to quantify the amount of solid mass in an elementary volume at time t (see Fig. 26). The elementary volumes thus contain the same amount of solid particles, then :

$$dz_{vol} = \phi_s \, d\zeta = \phi_0 \, da \tag{49}$$

With ϕ_0 is the initial solid volume fraction and ϕ_s is the solid volume fraction at a time $t > 0$.

Thus conversion from one coordinate system to another can be accomplished by simple integration such that :

$$z_{vol} = \int_0^a \phi_0 \, da \tag{50}$$

$$\zeta = \int_0^{z_{vol}} \frac{dz_{vol}}{\phi_s} \tag{51}$$

The Gibson equation derived in the main body of the article is expressed in the Eulerian coordinate meaning that we follow the change of ϕ_s at a given fixed position z as a function of time t. Doing so, we say that the changes in ϕ_s in time at a position z are caused by the inflow and outflow of matter at position z. The Lagrange form of the same equation gives the changes in ϕ_s for a given volume element that we follow in space and time. The reference settling velocity is the one of the solid particles. A direct result of this assumption is that the position z is a advective coordinate that depends on time and its reference position a at time $t = 0$:

$$z = \zeta(a, t) \tag{52}$$

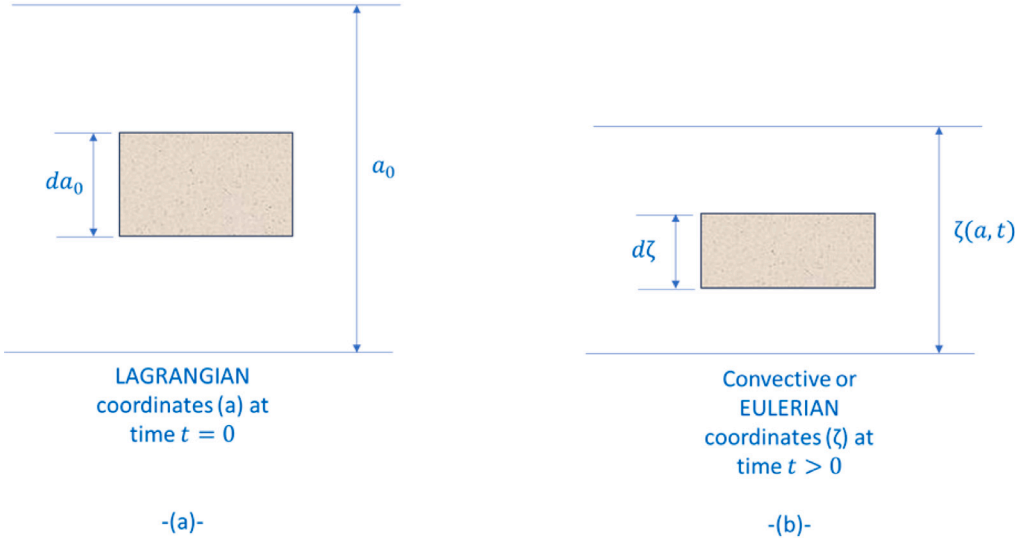

Fig. 25. At time $t = 0$, the system is given a configuration in what will be called the Lagrange coordinates as shown in the figure. The system is then referred to the "real" measurements as $t = 0$. For a time $t > 0$, during the consolidation process, "real" measurements are made in terms of convective coordinates that are a function of Lagrange coordinates. We assume that each measurement at any point can be linked to it initial value at time $t = 0$.

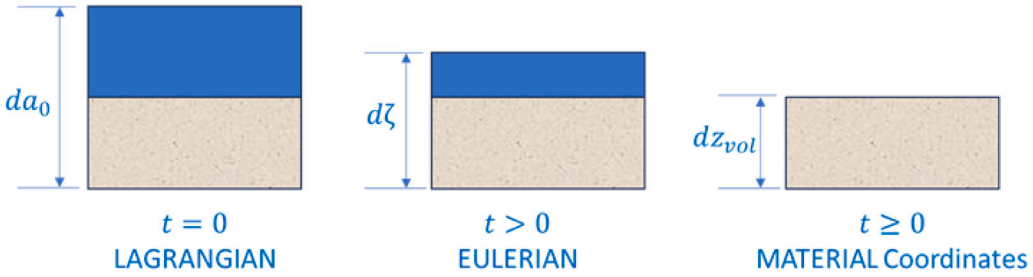

Fig. 26. Differential soil element chosen such that they encompass a unit volume of same solid particles in different coordinates.

The link between the Eulerian and Lagrange descriptions is given by :

$$\frac{d\phi_s}{dt} = \frac{\partial \phi_s}{\partial t} + v_{s/lab}\frac{\partial \phi_s}{\partial z} \tag{53}$$

where $\frac{d\phi_s}{dt}$ gives the Lagrange derivative and $\frac{\partial \phi_s}{\partial t}$ gives the Eulerian derivative. This equation tells us that the changes in ϕ_s of the volume element we follow and currently is located at $(z(a,t),t)$ is given by the change of ϕ_s (term $\frac{\partial \phi_s}{\partial t}$) at position $z(a,t)$ plus the change associated to the fact that the volume element we follow is leaving position z at the instant t (term $v_{s/lab}\frac{\partial \phi_s}{\partial z}$). In the Lagrange form the continuity equation can be written as :

$$\frac{d\phi_s}{dt} + \phi_s\frac{\partial v_{s/lab}}{\partial z} = 0 \tag{54}$$

Based on Eqs. (5), (9) and (54), we can express the Gibson equation in terms of total derivative:

$$\frac{d\phi_s}{dt} = \phi_s\frac{\partial}{\partial z}\left(\frac{K}{\rho_w g}\left(\frac{\partial \sigma_{sk}}{\partial z} + (\rho_s - \rho_w)g\phi_s\right)\right) \tag{55}$$

Now let express the equation in terms of the material coordinates z_{vol} to get the original form of the Gibson equation. We have :

$$\frac{d\phi_s}{dt} = \left(\frac{\partial \phi_s}{\partial t}\right)_{\zeta} = \left(\frac{\partial \phi_s}{\partial t}\right)_{z_{vol}} \tag{56}$$

The expression of the Gibson equation in the Lagrange frame is then :

$$\left(\frac{\partial \phi_s}{\partial t}\right)_{z_{vol}} = \phi_s^2\frac{\partial}{\partial z_{vol}}\left(\frac{K(\phi_s)}{\rho_w g}\phi_s\left(\frac{\partial \sigma_{sk}(\phi_s)}{\partial z_{vol}} + (\rho_s - \rho_w)g\right)\right) \tag{57}$$

Appendix B

B.1. Modified Gibson

We defined previously that there are two type fluxes in the column which are J_{adv} advection fluxes and J_{dif} diffusion fluxes that are in function of ϕ_s. Thus, when we reach the maximum compaction, it means mathematically that :

$$J_{\text{dif}}(\phi_s) = \begin{cases} \frac{K(\phi_s)}{g\rho_w}\frac{\partial \sigma_{sk}(\phi_s)}{\partial \phi_s}\frac{\partial \phi_s}{\partial z}\phi_s & \text{if } \phi_s \leq \phi_{\max} \\ 0 & \text{if } \phi_s > \phi_{\max} \end{cases} \tag{58}$$

$$J_{\text{adv}}(\phi_s) = \begin{cases} \frac{K(\phi_s)}{g\rho_w}(\rho_s - \rho_w)g\phi_s^2 & \text{if } \phi_s \leq \phi_{\max} \\ 0 & \text{if } \phi_s > \phi_{\max} \end{cases} \tag{59}$$

where ϕ_{max} is the maximum solid volume fraction.

Eqs. [(58)] and [(59)] can also be written as :

$$J_{\text{dif}}(\phi_s) = \frac{K(\phi_s)}{g\rho_w}\frac{\partial \sigma_{sk}(\phi_s)}{\partial \phi_s}\frac{\partial \phi_s}{\partial z}\phi_s 1_{[0,\phi_{max}]} \tag{60}$$

$$J_{\text{adv}}(\phi_s) = \frac{K(\phi_s)}{g\rho_w}(\rho_s - \rho_w)g\phi_s^2 1_{[0,\phi_{max}]} \tag{61}$$

With $1_{[0,\phi_{max}]}$ being the characteristic function defined as :

$$1_{[0,\phi_{max}]}(\phi_s) = \begin{cases} 1 & \text{if } \phi_s \leq \phi_{\max} \\ 0 & \text{if } \phi_s > \phi_{\max} \end{cases} \tag{62}$$

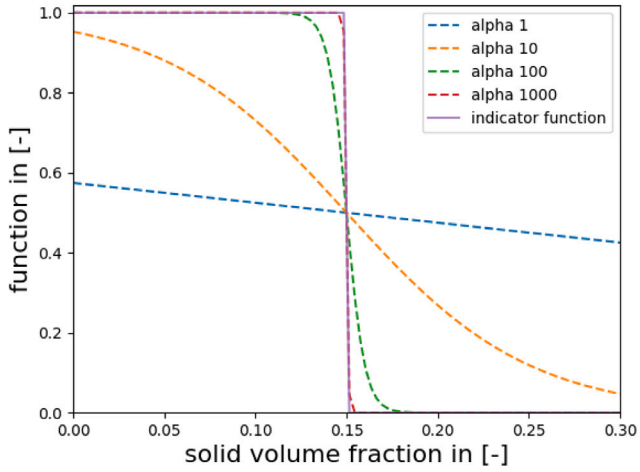

Fig. 27. The characteristic or indicator function approximation in 'purple solid line' using different values of parameter α of the sigmoid function represented by 'dashed lines'.

To make sure that the discontinuous nature of the characteristic function $1_{[0,\phi_{max}]}$ does not affect the numerical stability of the Gibson model, we approximate this function with a continuous function in the form of a sigmoid function $sigmoid_\alpha$:

$$sigmoid_\alpha(\phi_s) = \frac{1}{1+\exp(-\alpha(\phi_s - \phi_{max}))} \tag{63}$$

where α is a parameter without a unit.

The sigmoid function $sigmoid_\alpha$ converges to the characteristic function $1_{[0,\phi_{max}]}$ when α converges to infinity (see Fig. 27).

Appendix C. Supplementary data

Supplementary material related to this article can be found online at https://doi.org/10.1016/j.compgeo.2026.108200.

Data availability

No data was used for the research described in the article.

References

Abolfazli, E., Osborn, R., Dunne, K.B., Nittrouer, J.A., Strom, K., 2024. Flocculation characteristics of suspended Mississippi river mud under variable turbulence, water and salt sources, and salinity: A laboratory study. Front. Earth Sci. 12, 1268992.
Adachi, Y., Tanaka, Y., 1997. Settling velocity of an aluminium-kaolinite floc. Water Res. 31 (3), 449–454.
Ali, W., Chassagne, C., 2022. Comparison between two analytical models to study the flocculation of mineral clay by polyelectrolytes. Cont. Shelf Res. 250, 104864.
Ali, W., Enthoven, D., Kirichek, A., Helmons, R., Chassagne, C., 2022. Can flocculation reduce the dispersion of deep sea sediment plumes? In: Proceedings of the World Dredging Conference, Copenhagen, Denmark.
Almabruk, A., 2018. Sedimentation and consolidation of cohesive and non-cohesive soils formed under turbulent flows.
Barden, L., 1968. Primary and secondary conslidation of clay and peat. Geotechnique 18 (1), 1–24.
Bartholomeeusen, G., 2003. Compound Shock Waves and Creep Behaviour in Sediment Beds (Ph.D. thesis). Oxford University, UK.
Bartholomeeusen, G.S., 2003. Non-convex flux functions and compound shock waves in sediment beds. In: Hyperbolic Problems: Theory, Numerics, Applications: Proceedings of the Ninth International Conference on Hyperbolic Problems Held in CalTech, Pasadena, March 25–29, 2002. Springer, pp. 347–356.
Been, K., Sills, G., 1981. Self-weight consolidation of soft soils: an experimental and theoretical study. Geotechnique 31 (4), 519–535.
Brindley, G., 1958. Ion exchange in clay minerals. pp. 7–23.
Brownstein, K., Tarr, C., 1979. Importance of classical diffusion in NMR studies of water in biological cells. Phys. Rev. A 19 (6), 2446.
Chassagne, C., 2019. Understanding the natural consolidation of slurries using colloid science. In: 17th European Conference on Soil Mechanics and Geotechnical Engineering, ECSMGE 2019. International Society for Soil Mechanics and Geotechnical Engineering, pp. 1–8.
Chassagne, C., 2021. Introduction to colloid science: Applications to sediment characterization.
Davis, E., Raymond, G., 1965. A non-linear theory of consolidation. Geotechnique 15 (2), 161–173.
Dhont, J.K., 1996. An Introduction to Dynamics of Colloids. Elsevier.
Dietrich, W.E., 1982. Settling velocity of natural particles. Water Resour. Res. 18 (6), 1615–1626.
François, B., Corda, G., 2022. Experimental characterization and numerical modeling of the self-weight consolidation of a dredged mud. Geomech. Energy 29, 100274.
Geng, W., Han, W., Yin, J., Lu, Z., 2022. Salinity effects on the strength and morphological indices of soft marine clay. Sci. Rep. 12 (1), 17563.
Gibson, RE, G.H.M., 1967. The theory of one-dimensional consolidation of saturated clays: 1. finite non-linear consolidation of thin homogeneous layers. Geotechnique 17 (3), 261–273.
Guazzelli, E., Morris, J.F., 2011. A Physical Introduction to Suspension Dynamics. Vol. 45, Cambridge University Press.
Hol, N.J., Myouri, I., Chassagne, C., Pel, L., 2025. Determination of the surface relaxivity of soft sediment using particle size and shape. J. Magn. Reson. Open 100198.
Hol, N., Myouri, I., Chassagne, C., Pel, L., 2025. Determination of the surface relaxivity of soft sediment using particle size and shape. JMR Open 23, 100198.
Hol, N.J., Pel, L., Kurvers, M., Chassagne, C., 2024. Fast NMR imaging of clay sedimentation using a multi-slice stepper motor method. To be published, Unpublished work.
Hol, N.J., Pel, L., Kurvers, M., Chassagne, C., 2025. Fast 1D NMR imaging of clay sedimentation using a multi-slice stepper motor method. Exp. Fluids 66 (1), 9.
Hurley, S.J., 1999. Development of a Settling Column and Associated Primary Consolidation Monitoring Systems for Use in the Geotechnical Centrifuge: Investigation of Geotechnical-Geophysical Correlations (Ph.D. thesis). Memorial University of Newfoundland.
Kopinga, K., Pel, L., 1994. One-dimensional scanning of moisture in porous materials with NMR. Rev. Sci. Instrum. 65 (12), 3673–3681.
Lagaly, G., Dékány, I., 2013. Colloid clay science. In: Developments in Clay Science. vol. 5, Elsevier, pp. 243–345.
Meiboom, S., Gill, D., 1958. Modified spin-echo method for measuring nuclear relaxation times. Rev. Sci. Instrum. 29 (8), 688–691.
Merckelbach, Kranenburg, W.J., 2002. Strength modelling of consolidating mud beds. In: Proceedings in Marine Science. vol. 5, Elsevier, pp. 359–373.
Mikasa, M., 1963. Consolidation theory for nonhomogeneous clay layer. In: Proc. of Autumn Convention of JSSMFE. pp. 41–43.
Pel, L., Donkers, P., Kopinga, K., Noijen, J., 2016. ^{1}H, ^{23}na and ^{35}cl imaging in cementitious materials with NMR. Appl. Magn. Reson. 47 (3), 265–276.
Poiseuille, J.L., 1844. Recherches Expérimentales Sur Le Mouvement Des Liquides Dans Les Tubes De Très-Petits Diamètres. Imprimerie Royale.
Pu, H., Song, D., Fox, P.J., 2018. Benchmark problem for large strain self-weight consolidation. J. Geotech. Geoenvironmental Eng. 144 (5), 06018002.
Pu, H., Wang, K., Qiu, J., Chen, X., 2020. Large-strain consolidation modeling of soft soils considering nonlinear properties. J. Geotech. Geoenvironmental Eng. 146 (6), 04020049.
Rial, M.B., 2019. Consolidation and drying of slurries: A building with nature study for the marker wadden.
Richardson, J., Zaki, W., 1997. Sedimentation and fluidisation: Part i. Chem. Eng. Res. Des. 75, S82–S100.
Robinson, R.G., Allam, M.M., 1998. Effect of clay mineralogy on coefficient of consolidation. Clays Clay Miner. 46 (5), 596–600.
van Roij, R., 2003. Defying gravity with entropy and electrostatics: sedimentation of charged colloids. J. Phys.: Condens. Matter. 15 (48), S3569.
Roscoe, K.H., Schofield, A., Wroth, a.P., 1958. On the yielding of soils. Geotechnique 8 (1), 22–53.
Russel, W.B., Saville, D.A., Schowalter, W.R., 1989. Colloidal Dispersions. Cambridge University Press, Cambridge.
Schiffman, R.L., Gibson, R.E., 1964. Consolidation of nonhomogeneous clay layers. J. the Soil Mech. Found. Div. 90 (5), 1–30.
Schofield, R., Samson, H., 1954. Flocculation of kaolinite due to the attraction of oppositely charged crystal faces. Discuss. Faraday Soc. 18, 135–145.
Shakeel, A., Ali, W., Chassagne, C., Kirichek, A., 2022. Tuning the rheological properties of kaolin suspensions using biopolymers. Colloids Surfaces A: Physicochem. Eng. Asp. 654, 130120.
Tafili, M., Duque, J., Sutter, I., Mašín, D., 2026. Influence of pore-fluid salinity on the monotonic and cyclic behavior of Scheruhn kaolin. Can. Geotech. J..
Terzaghi, K., 1925. Erdbaumechanik auf bodenphysikalischer Grundlage. F. Deuticke.

Valckenborg, R., Pel, L., Hazrati, K., Kopinga, K., Marchand, J., 2001. Pore water distribution in mortar during drying as determined by NMR. Mater. Struct. 34 (10), 599–604.

Wang, J., Yuan, W., Yin, X., Li, W., Li, X., 2023. One-dimensional consolidation properties of soft clay under multi-stage loading. Appl. Sci. 13 (18), 10340.

Watabe, Y., Yamada, K., Saitoh, K., 2011. Hydraulic conductivity and compressibility of mixtures of Nagoya clay with sand or bentonite. Géotechnique 61 (3), 211–219.

Zanin, R.F., Padilha, A.C., Pelaquim, F.G., Gutierrez, N.H., Teixeira, R.S., 2021. The effect of pH and electrical conductivity of the soaking fluid on the collapse of a silty clay. Soils Rocks 44, e2021061620.